

Nonlinear stability and structure of compressible reacting mixing layers

By M. J. DAY¹, N. N. MANSOUR² AND W. C. REYNOLDS¹

¹Department of Mechanical Engineering, Stanford University, Stanford, CA 94035-3030, USA

²NASA Ames Research Center, Moffett Field, CA 94035-1000, USA

(Received 21 July 2000 and in revised form 31 May 2001)

The parabolized stability equations (PSE) are used to investigate issues of non-linear flow development and mixing in compressible reacting shear layers, which are modelled with an infinitely fast-chemistry assumption. Particular emphasis is placed on investigating the change in flow structure that occurs when compressibility and heat release are added to the flow. These conditions allow the ‘outer’ instability modes—one associated with each of the fast and slow streams—to dominate over the ‘central’, Kelvin–Helmholtz mode that exists unaccompanied in incompressible non-reacting mixing layers. Analysis of scalar probability density functions in flows with dominant outer modes demonstrates the ineffective, one-sided nature of mixing that accompanies these flow structures. Colayer conditions, where two modes have equal growth rate and the mixing layer is formed by two sets of vortices, offer some opportunity for mixing enhancement. Their extent, however, is found to be limited in the mixing layer’s parameter space. Extensive validation of the PSE technique also provides a unique perspective on central-mode vortex pairing, further supporting the view that pairing is primarily governed by instability growth rates; mutual induction appears to be a secondary process. This perspective sheds light on how linear stability theory is able to provide such an accurate prediction of experimentally observed, fully nonlinear flow phenomenon.

1. Introduction

Direct and efficient mixing of fuel and oxidizer streams is of primary interest in all combustion applications. This is particularly true in flows that combine significant heat release with compressible shear, where these two influences can cause a substantial change in the large-scale flow structure and hence in the mixing characteristics. An intuitive understanding of these flow-structure changes that occur in compressible reacting mixing layers can be developed by examining the density-weighted vorticity profile, $\rho du/dy$. The shape of this profile is shown in figure 1 for (a) incompressible non-reacting and (b) compressible reacting conditions. The former conditions result in uniform cross-stream density and a single, centrally located peak in the $\rho du/dy$ profile. This results in the familiar type of two-dimensional flow structure that was first experimentally identified by Brown & Roshko (1974) and corresponds to the Kelvin–Helmholtz instability. This coherent structure, which dominates incompressible non-reacting mixing layers, will be used as a convenient reference point in this work, referred to as the ‘central’ mode based on its general location in the layer.

This mixing configuration changes dramatically when the influences of compressibility and chemical reaction are considered. Both of these factors will cause an

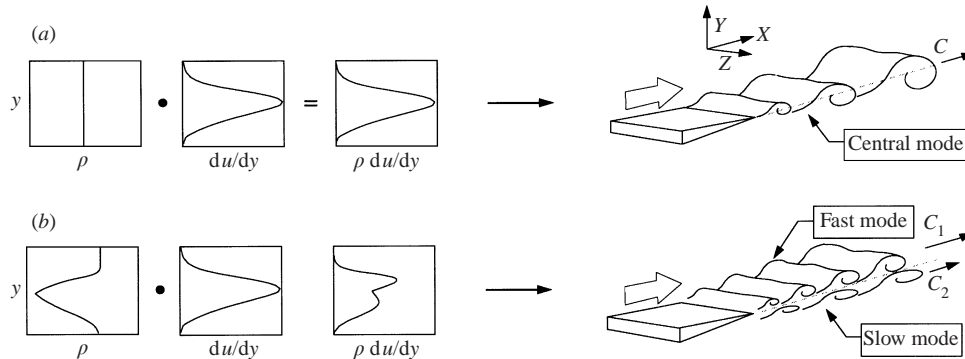


FIGURE 1. Construction of the density-weighted vorticity profile and the resulting flow structure in (a) incompressible non-reacting and (b) compressible reacting conditions.

increase in temperature along the centreline: compressibility through the coupling of kinetic and thermal energy, and chemical reaction through the enthalpy of combustion. The result, as shown in figure 1(b), is a drop in density along the centreline and a transition in the shape of the $\rho du/dy$ profile from a single- to double-peak appearance. Correspondingly, two new instability modes—referred to individually as ‘fast’ and ‘slow’ and jointly as ‘outer’ modes—can become dominant.

An appreciation of the importance of large-scale, organized flow structures follows from Brown & Roshko’s (1974) discovery of the dominant role these vortical structures play in mixing processes. Therefore, developing an understanding of the flow-structure changes induced by compressibility and heat release is critically important to applications of supersonic combustion, scramjets in particular. Outer-mode flow structures also provide the physics behind flame flicker in buoyant diffusion flames (Chen *et al.* 1988), and can possibly provide an explanation for measurements of structure convection speeds that indicate a migration in velocity toward the free-stream limits in supersonic flows (Papamoschou & Bunyajitradulya 1997; Smith & Dutton 1999).

1.1. Background

The central mode provides a convenient and well-studied reference point for our discussion. A comprehensive overview of early experimental and computational work done in the low-compressibility regime is provided by Ho & Huerre (1984). Studies particularly relevant to our work include Winant & Browand’s (1974) observation that successive pairing between neighbouring vortices forms the dominant mechanism for mixing-layer growth. Clemens & Mungal (1995) demonstrated that this remained a critical mechanism at high Reynolds number. Central-mode mixing properties were investigated by Konrad (1976), Koochesfahani & Dimotakis (1986) and Masutani & Bowman (1986), all of whom identified a preferred mixture fraction value, ξ , that is governed by the entrainment ratio and demonstrates a bias toward the fast-free-stream fluid. These studies also found that pure free-stream fluid from both free streams could be transported throughout the layer by large-scale structures without mixing.

The stabilizing effect of compressibility on the central-mode growth rate was first observed in the linear stability studies of Dunn & Lin (1955), Lessen, Fox & Zien (1965) and Gropengiesser (1970). Experimental evidence for the growth rate suppression built on the results of Brown & Roshko (1974), who were the first to separate density ratio and compressibility effects. For mixing layer flows,

more definitive evidence came from the experiments of Chinzei *et al.* (1986) and Papamoschou & Roshko (1988). An explanation for this reduction was provided by Vreman, Sandham & Luo (1996) with the use of DNS databases at various compressibilities and a growth-rate model based on the integrated production of turbulent kinetic energy. They demonstrated that suppression of the pressure–strain–redistribution term, caused by the reduction of pressure fluctuations, was responsible for the growth rate attenuation with compressibility. The early stability work of Dunn & Lin (1955), Lessen *et al.* (1965) and Gropengiesser (1970) also identified three-dimensionality as a second manifestation of compressibility. Subsequent numerical studies by Sandham & Reynolds (1991) found that the transition from two- to three-dimensionality starts at a convective Mach number, M_c (see definition below), of 0.6, which was experimentally verified by Clemens & Mungal (1995).

The third important contribution from compressible stability work was the identification of two additional instability modes, one associated with each of the fast and slow streams (Lessen, Fox & Zien 1966; Gropengiesser 1970). These ‘supersonic’ stability modes, fully characterized by Jackson & Grosch (1989), were predicted to exist at compressibility regimes unattainable in most experimental facilities. Further, their growth rates were found to be lower than the three-dimensional central mode, and hence they were originally viewed to be of more theoretical than practical interest. However, this perspective changes considerably when the influence of combustion is considered; now, as explained earlier, both compressibility and heat release can work together to cause outer-mode dominance (Jackson & Grosch 1990; Planché 1992; Planché & Reynolds 1992; Shin & Ferziger 1993). Indeed, Jackson & Grosch (1990) point out that, taken separately, the influences of compressibility and heat release on creating outer modes are quite similar. A full characterization of the different modal regimes—central, fast and slow—that exist in the mixing layer’s parameter space is provided in Day, Mansour & Reynolds (1998). The outer-mode creation mechanism, based on the $\rho du/dy$ profile, applies equally to all shear layers; Papas, Monkewitz & Tomboulides (1999) investigated the stability characteristics of similar ‘heat release’ modes in a diffusion flame using finite-rate chemistry.

Experimental work in compressible reacting conditions is limited due to its considerable complexity. Significant work on compressible reacting mixing layers at $M_c > 0.4$ has been reported by Miller, Bowman & Mungal (1998), although their combination of heat release and compressibility was not sufficient to generate dominant outer modes (Planché 1992, see also Planché & Reynolds 1992). However, these experiments did indicate, in agreement with Hall (1991), that compressibility removes the fast-side bias in the entrainment rate of the central mode. Also, Miller *et al.* (1998) noted a significant increase in OH signal between their low- ($M_c = 0.32, 0.35$) and high-compressibility ($M_c = 0.70$) cases, suggesting that the development of three-dimensional flow structure in the latter case enhanced the combustion process. Experiments to access outer-mode regimes have been planned by Rossmann, Hanson & Mungal (1999).

The motivation behind the current study becomes clear when mixing mechanisms of the central and outer modes are compared. The central mode efficiently entrains fuel from one side of the layer and oxidizer from the other (see figure 2*a*). The single-step nature of this mixing process is in contrast to the outer-mode mechanism shown in figure 2*b*). Here, each instability mode mixes one reactant into the combustion zone, resulting in a two-step process. Preliminary DNS calculations of Planché (1992) indicated a significantly lower global reaction rate with this flow configuration when compared to the central-mode case of figure 2*a*). Further, these calculations and

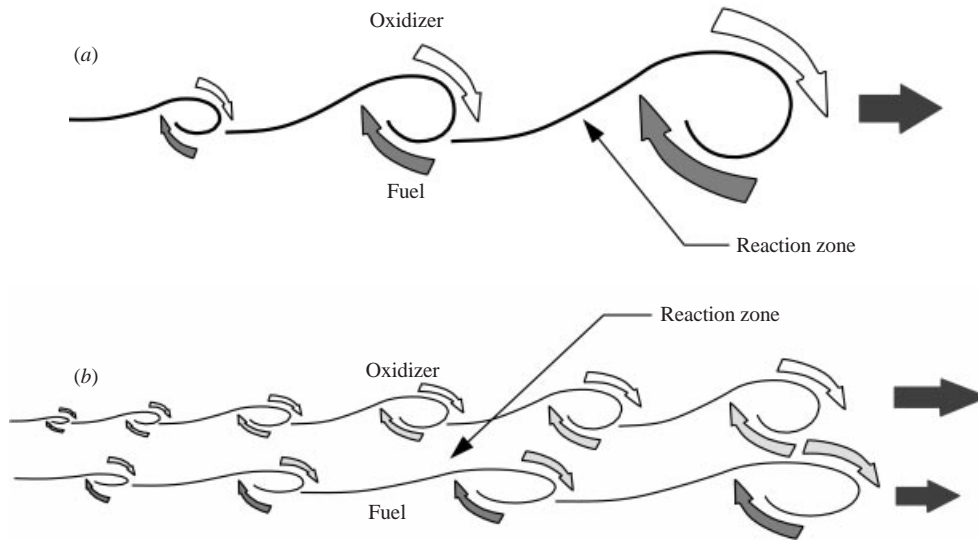


FIGURE 2. Schematic of the mixing mechanism in (a) central- and (b) outer-mode-dominated flows.

the outer-mode schematic drawn here refer to the ‘colayer’ case, where both outer vortical modes are present; combustion performance further deteriorates when flow conditions change and only a single outer mode remains (Day *et al.* 1998).

The primary objective of this paper is to provide a comparison of mixing performance and flow physics between outer-mode-dominated flows—in both single mode and colayer configurations—and the more commonly studied central-mode mixing layer. The conflicting requirements to analyse a number of three-dimensional computational solutions while maintaining a reasonable computational cost motivated our use of the parabolized stability equations (PSE). For the regime of convectively unstable flows, this technique provides a tool for modelling nonlinear and non-parallel effects that are critical to the accurate simulation of large-scale structure. Understandably, the mode-limited nature of this analysis technique restricts our analysis to large-scale structures and their associated mixing processes.

With a focus on brevity, the main principles of the PSE technique are outlined in §2—its details appear in Day (1999; see also Day, Mansour & Reynolds 1999). As the first application of this technique to mixing layer flows, validation against DNS results is provided in §3 for both sub- and supersonic flow regimes. Interestingly, this validation also provides a unique perspective on central-mode vortex pairing, offering a compelling explanation for how linear stability analysis is able to effectively predict fully nonlinear flow phenomenon. Section 4 addresses a comparison of central- and outer-mode mixing performance, and also evaluates strategies for mixing enhancement in a colayer flow structure.

2. Numerical methodology

2.1. Flow parameters

A schematic of the flow configuration is shown in figure 3. The high-speed stream on the upper side of the mixing layer (denoted with the subscript 1) carries a mass

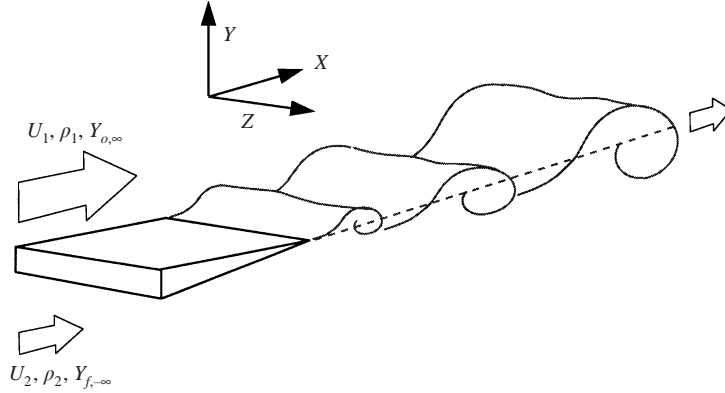


FIGURE 3. Schematic of the flow configuration with specified input conditions.

fraction of oxidizer, $Y_{0,\infty}$, while the slow-speed stream (subscript 2) carries a mass fraction of fuel, $Y_{f,-\infty}$. The density, ρ , can vary between the two streams.

The current work follows convention in using the convective Mach number (Bogdanoff 1983; Papamoschou & Roshko 1988) as a generalized measure of compressibility. This parameter has the definition

$$M_c = \frac{U_1^* - U_2^*}{a_1^* + a_2^*} \quad (2.1)$$

for flows of uniform specific heats, where U_1, a_1 and U_2, a_2 are the velocity and sound speed of the fast and slow free streams, and (*) denotes a dimensional quantity.

Chemical reactions in this investigation are simplified using the approximation of a single, infinitely fast step of the form



where n represents the mass of oxidizer that stoichiometrically reacts with one unit-mass of fuel to produce $n + 1$ unit masses of product. The amount of heat release imparted to the layer is measured through a non-dimensionalized enthalpy of combustion (heat release parameter)

$$\Theta = \frac{-\Delta H_c^* Y_{f,-\infty}}{c_{p1}^* \bar{T}_1^* (1 + \phi)} \quad (2.3a)$$

$$= \frac{-[(n + 1)\Delta h_{f,p}^{*,o} - n\Delta h_{f,o}^{*,o} - \Delta h_{f,f}^{*,o}] Y_{f,-\infty}}{c_{p1}^* \bar{T}_1^* (1 + \phi)} \quad (2.3b)$$

$$= T_f - 1, \quad (2.3c)$$

where ΔH_c^* is the enthalpy of combustion per unit mass of fuel, $Y_{f,-\infty}$ is the fuel mass fraction on the slow side, c_{p1}^* is the specific heat, $\Delta h_{f,k}^{*,o}$ is the enthalpy of formation for species k , and \bar{T}_1^* the temperature on the fast side of the mixing layer. With this definition, the heat release parameter has the concise relation to the adiabatic flame temperature, T_f , given in equation (2.3c) (Williams 1985). The equivalence ratio is also included in the Θ -equation, and its definition is

$$\phi = \frac{(Y_{f,-\infty}/Y_{0,\infty})_{\text{real}}}{(Y_{f,-\infty}/Y_{0,\infty})_{\text{stoich}}} = \frac{nY_{f,-\infty}}{Y_{0,\infty}}, \quad (2.4)$$

where n is specified in equation (2.2). The remaining parameters of the investigation are the free-stream density and velocity ratios, $s = \rho_2^*/\rho_1^*$ and $r = U_2^*/U_1^*$.

2.2. Mean-flow solution

Stability analysis – both parabolized and linear – requires the input of mean velocity and temperature profiles. Their solution begins with the two-dimensional compressible boundary layer equations for laminar reacting flow. Starting with these equations (see, for example, Kuo 1986), all quantities are non-dimensionalized by their respective values on the high-speed side of the layer with the vorticity thickness $\delta_\omega = \Delta U/|d\bar{u}/dy|_{\max}$ serving as the length scale. The equations are further simplified by assuming unity Prandtl and Lewis numbers and negligible streamwise pressure gradient. These simplifications yield the following non-dimensional system for continuity, streamwise momentum, energy, species mass fraction, and the ideal gas equation of state:

$$\frac{\partial \rho u}{\partial x} + \frac{\partial \rho v}{\partial y} = 0, \quad (2.5a)$$

$$\rho u \frac{\partial u}{\partial x} + \rho v \frac{\partial u}{\partial y} = \frac{1}{Re_o} \frac{\partial}{\partial y} \left(\mu \frac{\partial u}{\partial y} \right), \quad (2.5b)$$

$$\rho u \frac{\partial h_t}{\partial x} + \rho v \frac{\partial h_t}{\partial y} = \frac{1}{Re_o} \frac{\partial}{\partial y} \left(\mu \frac{\partial h_t}{\partial y} \right), \quad (2.5c)$$

$$\rho u \frac{\partial Y_k}{\partial x} + \rho v \frac{\partial Y_k}{\partial y} = \frac{1}{Re_o} \frac{\partial}{\partial y} \left(\mu \frac{\partial Y_k}{\partial y} \right) + \dot{w}_k, \quad (2.5d)$$

$$\rho RT = 1, \quad (2.5e)$$

where x and y are the streamwise and normal coordinate directions; u and v are the velocity components in those directions; ρ , p and T are the density, pressure, and temperature, respectively; μ is the viscosity; Y_k is the mass fraction of species k , where k is one of oxidizer, fuel or product; \dot{w}_k is the time rate of production of species k ; R is the gas constant; and energy is cast in terms of the total enthalpy, h_t^* , to capture both internal and kinetic forms of energy.

Further simplification of these equations is achieved by introducing the stream function definition for compressible flow, $\rho u = \partial \psi / \partial y$ and $\rho v = -\partial \psi / \partial x$, which eliminates the continuity equation (2.5a), and through the single-step, infinitely fast chemistry assumption of equation (2.2). The resulting equations for conservation of momentum, species (cast using the passive scalar $Z = Y_f - Y_o/n$), and energy then appear as

$$\frac{\partial \psi}{\partial y} \frac{\partial u}{\partial x} - \frac{\partial \psi}{\partial x} \frac{\partial u}{\partial y} = \frac{1}{Re_o} \frac{\partial}{\partial y} \left(\mu \frac{\partial u}{\partial y} \right), \quad (2.6a)$$

$$\frac{\partial \psi}{\partial y} \frac{\partial Z}{\partial x} - \frac{\partial \psi}{\partial x} \frac{\partial Z}{\partial y} = \frac{1}{Re_o} \frac{\partial}{\partial y} \left(\mu \frac{\partial Z}{\partial y} \right), \quad (2.6b)$$

$$\frac{\partial \psi}{\partial y} \frac{\partial h_t}{\partial x} - \frac{\partial \psi}{\partial x} \frac{\partial h_t}{\partial y} = \frac{1}{Re_o} \frac{\partial}{\partial y} \left(\mu \frac{\partial h_t}{\partial y} \right). \quad (2.6c)$$

A similarity solution can be found by first introducing Howarth's coordinate transformations (Schlichting 1979)

$$\zeta = x \quad \text{and} \quad \eta = \sqrt{\frac{Re_o}{2x}} \int_0^y \rho dy. \quad (2.7)$$

Then, by assuming that the mixing layer is fully developed and that quantities are only dependent on η , we have

$$\psi(x, y) = \sqrt{\frac{2x}{Re_o}} F(\eta), \quad Z(x, y) = Z(\eta), \quad h_t(x, y) = h_t(\eta). \quad (2.8)$$

The additional, but not required, assumption that the non-dimensional viscosity and temperature are linearly related yields the further simplified form

$$F''' + FF'' = 0, \quad Z'' + FZ' = 0, \quad h_t'' + Fh_t' = 0, \quad (2.9)$$

where ' denotes differentiation with respect to η .

This system of equations is solved using the shooting method of Sandham (1989; see also Sandham & Reynolds 1989) with refinements discussed in Day (1999), subject to the boundary conditions

$$F'(\infty) = U_1, \quad F(0) = 0, \quad F'(-\infty) = U_2, \quad (2.10a)$$

$$Z(\infty) = -Y_{0,\infty}/n, \quad Z(-\infty) = Y_{f,-\infty}, \quad (2.10b)$$

$$h_t(\infty) = \frac{\gamma RT_1}{(\gamma - 1)M_1} + Y_{o,\infty}\Delta h_{f,o}^o + U_1^2/2, \quad (2.10c)$$

$$h_t(-\infty) = \frac{\gamma RT_2}{(\gamma - 1)M_1} + Y_{f,-\infty}\Delta h_{f,f}^o + U_2^2/2, \quad (2.10d)$$

where the latter two equations appear with the assumption of constant specific heats, $\gamma = \gamma_1 = \gamma_2 = 1.4$, and uniform molecular mass, \mathcal{M} , in the mixing layer. The uniform-molecular-mass assumption yields a uniform gas constant and, more importantly, a reciprocal relationship between ρ and T through the ideal gas equation and the thin-shear-layer assumption of uniform pressure.

With the solutions for $F(\eta)$, $h_t(\eta)$ and $Z(\eta)$ at hand, the mean u and v profiles are available from equation (2.8), while the temperature profiles are evaluated from

$$T(x, y) = (h_t(\eta) - Y_f(\eta)\Delta h_{f,f}^o - Y_o(\eta)\Delta h_{f,o}^o - u^2(\eta)/2) / c_p. \quad (2.11)$$

The heats of formation are determined from equation (2.3b) for a prescribed value of Θ with the assumption that the chemical reference species includes both the product and oxidizer, and hence $\Delta h_{f,f}^o$ is the only non-zero contribution to ΔH_c .

2.3. Parabolized stability equations

The parabolized stability equations (PSE) were conceived (Herbert & Bertolotti 1987; Bertolotti, Herbert & Spalart 1992; Herbert 1994) as a tool that, for the limited class of convectively unstable shear flows, would provide the quantitative accuracy of large-eddy or direct simulation while maintaining low computational cost and significant flexibility. The advantages of this technique stem from the fact that it is nonlinear and non-parallel, implying better physical representation and greater quantitative accuracy than linear, parallel stability techniques.

Derivation of the PSE begins with the decomposition of flow variables into mean and fluctuating parts:

$$\left. \begin{aligned} \rho &= \bar{\rho} + \tilde{\rho}, & T &= \bar{T} + \tilde{T}, & p &= 1 + \tilde{p}, & Z &= \bar{Z} + \tilde{Z}, \\ u &= \bar{u} + \tilde{u}, & v &= \bar{v} + \tilde{v}, & w &= 0 + \tilde{w}, \end{aligned} \right\} \quad (2.12)$$

where the non-dimensional pressure is assumed uniform in the solution domain and the mean flow in the spanwise direction (the w -component) is neglected. Again, we

make use of the passive scalar, $Z = Y_f - Y_o/n$, and the infinitely fast, one-step reaction model of equation (2.2).

Our original development of the PSE employed the inviscid equations for momentum, energy and species, in addition to the continuity and state equations that are required to close the system. However, for reasons that will be explained, the numerical stability of the PSE approach is enhanced by the inclusion of viscous terms in the cross-stream direction; the net result amounts to the use of the thin-shear-layer equations for our analysis. With the assumption of constant specific heats and molecular mass, these governing equations can be expressed in non-dimensional form as

$$\frac{\partial \rho}{\partial t} + \frac{\partial \rho u_i}{\partial x_i} = 0, \quad (2.13a)$$

$$\rho \left(\frac{\partial u_i}{\partial t} + u_j \frac{\partial u_i}{\partial x_j} \right) = -\frac{1}{\gamma_1 M_1^2} \frac{\partial p}{\partial x_i} + \frac{1}{Re_o} \frac{\partial \tilde{\tau}_{ij}}{\partial x_j}, \quad (2.13b)$$

$$\rho \left(\frac{\partial Z}{\partial t} + u_i \frac{\partial Z}{\partial x_i} \right) = \frac{\mu}{Re_o Sc} \frac{\partial}{\partial x_i} \left(\mu \frac{\partial Z}{\partial x_i} \right), \quad (2.13c)$$

$$\rho \left(\frac{\partial T}{\partial t} + u_i \frac{\partial T}{\partial x_i} \right) = \frac{\gamma}{Pr Re_o} \frac{\partial}{\partial x_i} \left(\mu \frac{\partial T}{\partial x_i} \right) - p(\gamma - 1) \frac{\partial u_i}{\partial x_i}, \quad (2.13d)$$

$$p = \rho T, \quad (2.13e)$$

where Pr and Sc are the Prandtl and Schmidt numbers, and

$$\frac{\partial \tilde{\tau}_{ij}}{\partial x_j} = \begin{cases} \frac{\partial}{\partial y} \left(\mu \frac{\partial u}{\partial y} \right) & \text{if } i = 1, j = 2, \\ \frac{4}{3} \frac{\partial}{\partial y} \left(\mu \frac{\partial v}{\partial y} \right) & \text{if } i = 2, j = 2, \\ \frac{\partial}{\partial y} \left(\mu \frac{\partial w}{\partial y} \right) & \text{if } i = 3, j = 2, \\ 0 & \text{otherwise.} \end{cases} \quad (2.14)$$

Substituting the decompositions of equation (2.12) into the governing system of equation (2.13) and subtracting mean-flow terms yields

$$\mathbf{\Gamma} \frac{\partial \tilde{\boldsymbol{\phi}}}{\partial t} + \mathbf{A} \frac{\partial \tilde{\boldsymbol{\phi}}}{\partial x} + \mathbf{B} \frac{\partial \tilde{\boldsymbol{\phi}}}{\partial y} + \mathbf{C} \frac{\partial^2 \tilde{\boldsymbol{\phi}}}{\partial y^2} + \mathbf{D} \frac{\partial \tilde{\boldsymbol{\phi}}}{\partial z} + \mathbf{E} \tilde{\boldsymbol{\phi}} = \mathbf{F}, \quad (2.15)$$

where $\tilde{\boldsymbol{\phi}} = [\tilde{\rho}, \tilde{u}, \tilde{v}, \tilde{w}, \tilde{Z}, \tilde{T}, \tilde{p}]^T$ is the perturbation vector, and the right-hand-side term \mathbf{F} represents the nonlinear terms.

Disturbances are assumed to be periodic in both time and spanwise dimensions, which permits a Fourier representation

$$\tilde{\boldsymbol{\phi}}(x, y, z, t) = \sum_{m=-\infty}^{\infty} \sum_{n=-\infty}^{\infty} \hat{\boldsymbol{\phi}}_{mn}(x, y) e^{i(\beta_n z - \omega_m t)}, \quad (2.16)$$

where, for base frequency ω_1 and spanwise wavenumber β_1 , $\omega_m = m\omega_1$ and $\beta_n = n\beta_1$.

In practice, the modes are truncated to a finite number of order 10:

$$\tilde{\phi}(x, y, z, t) = \sum_{m=-M}^M \sum_{n=-N}^N \hat{\Phi}_{mn}(x, y) e^{i(\beta_n z - \omega_m t)}. \quad (2.17)$$

(In addition, we note that the summations also must include additional modes for dealiasing according to the three-halves rule.) The PSE approach borrows from the more limited multiscale method by decomposing $\hat{\Phi}_{mn}$ into a slowly varying shape function and a rapidly varying wave-like part to obtain

$$\hat{\Phi}_{mn}(x, y) = \hat{\phi}_{mn}(x, y) \mathcal{A}_{mn}(x), \quad (2.18)$$

where

$$\mathcal{A}_{mn}(x) = \epsilon_{o_{mn}} \exp\left(i \int_0^x \alpha_{mn}(x') dx'\right) \quad (2.19)$$

is the amplification factor, $\epsilon_{o_{mn}}$ is the initial disturbance magnitude, $\hat{\phi}_{mn}$ is the vector of shape functions, and α_{mn} is the streamwise wavenumber. (We note that no summation is to be implied by repeated indices in this subsection.)

Substituting equations (2.17) to (2.19) into (2.15) results in the form

$$\mathcal{L}_{mn}(\hat{\phi}_{mn}) = \frac{\hat{F}_{mn}}{\mathcal{A}_{mn}}, \quad (2.20)$$

where

$$\mathcal{L}_{mn} = -i\omega_{mn}\mathbf{\Gamma} + \mathbf{A}(i\alpha_{mn} + \frac{\partial}{\partial x}) + \mathbf{B} \frac{\partial}{\partial y} + \mathbf{C} \frac{\partial^2}{\partial y^2} + i\beta_{mn}\mathbf{D} + \mathbf{E}.$$

For efficiency, the Fourier forcing component, \hat{F}_{mn} , is evaluated through a fast Fourier transform of the total forcing vector, \mathbf{F} , which is evaluated in real space. This transform appears as,

$$\mathbf{F}(x, y, z, t) = \sum_{m=-M}^M \sum_{n=-N}^N \hat{F}_{mn}(x, y) e^{i(n\beta_1 z - m\omega_1 t)}. \quad (2.21)$$

The PSE formulation employs three techniques for obtaining greater computational efficiency than through direct numerical simulation. First, the streamwise-fluctuating shape of the disturbance is assumed, thereby avoiding the use of a fine-resolution grid in the streamwise direction. Second, the Fourier series of (2.17) is severely truncated to limit analysis to the large scales where these assumptions are valid. And, most importantly, the slowly varying assumption applied to the shape function is expressed as $\partial^2 \hat{\phi}_{mn} / \partial x^2 = 0$, rendering the governing equations ‘nearly’ parabolic (to be explained below) regardless of whether the thin-shear-layer or full equations are used. This permits a streamwise marching solution for $\hat{\phi}_{mn}$. Our analysis also makes a further simplification by applying a symmetry condition in the spanwise direction about $z = 0$. Together, these aspects of the PSE combine to result in a technique that is extremely efficient and accurate in simulating the flow development to a moderately nonlinear stage.

An analysis of equation (2.18) reveals that the streamwise change of $\hat{\Phi}(x, y)$ can be absorbed into either the shape function, $\hat{\phi}(x, y)$, or the streamwise wavenumber, $\alpha(x)$, where the latter defines the value of the amplitude function, $\mathcal{A}(x)$. This ambiguity must be resolved through the introduction of an additional equation; one commonly employed solution is to impose a constraint on the streamwise growth of $\hat{\phi}(x, y)$. The

particular choice of constraint appears to only have a slight quantitative effect on PSE results. The method proposed by Herbert (1994) has the benefit of a mathematical basis and an integral approach, and it is employed in this investigation. Briefly, it evolves by considering the streamwise logarithmic derivative of equation (2.17)

$$-i(\ln \hat{\phi})_x = \alpha - i \frac{\hat{\phi}_x}{\hat{\phi}}. \quad (2.22)$$

It is desirable to equate this result with what would be obtained in the case of a linear stability formulation, which lacks the second term, in order to equate growth-rate definitions. This term can be eliminated in an integral sense by multiplying both sides of equation (2.22) by $|\hat{\phi}|^2$, integrating over the $\bar{\mathcal{U}}$ domain in y , and dividing by the integral of $|\hat{\phi}|^2$. The procedure yields

$$-i \frac{\int_{\bar{\mathcal{U}}} |\hat{\phi}|^2 (\ln \hat{\phi})_x dy}{\int_{\bar{\mathcal{U}}} |\hat{\phi}|^2 dy} = \alpha - i \frac{\int_{\bar{\mathcal{U}}} \hat{\phi}^\dagger \hat{\phi}_x dy}{\int_{\bar{\mathcal{U}}} |\hat{\phi}|^2 dy}, \quad (2.23)$$

where \dagger denotes a complex conjugate. The second term can be eliminated by choosing

$$\int_{\bar{\mathcal{U}}} \hat{\phi}^\dagger \hat{\phi}_x dy = 0 \quad (2.24)$$

as the integral norm to close the PSE system. In the calculations to follow, only the velocity-component contributions to the vector $\hat{\phi}$ are included, yielding the norm

$$\int_{\bar{\mathcal{U}}} \hat{\mathbf{v}}^\dagger \hat{\mathbf{v}}_x dy = 0, \quad (2.25)$$

where $\hat{\mathbf{v}} = (\hat{u}, \hat{v}, \hat{w})$.

To this point in the analysis, the governing equation (2.20) has been described as parabolic without further justification. However, the analyses of Haj-Hariri (1994) and, in greater detail, of Li & Malik (1996) and Andersson, Henningson & Hanifi (1998) have identified residual ellipticity in the parabolized equations that make them ill-posed for a streamwise marching solution. The majority of this ellipticity arises from the $\partial \hat{p} / \partial x$ term, which physically represents the upstream acoustic wave, and can manifest itself by destabilizing the marching procedure in subsonic flows. The approach taken herein is to introduce a damping function, Ω , to eliminate the primary source of upstream influence found in the streamwise pressure gradient:

$$\frac{\partial p'}{\partial x} = \sum_{m=-M}^M \sum_{n=-N}^N \left(i\alpha_{mn} \hat{p}_{mn} + \Omega \frac{\partial \hat{p}_{mn}}{\partial x} \right) \mathcal{A}_{mn}(x) e^{i(\beta_n z - \omega_m t)}. \quad (2.26)$$

We note that even the coarse assumption of setting $\Omega = 0$ eliminates, at worst, a secondary part of the streamwise derivative because \hat{p}_{mn} is slowly varying in the streamwise direction. This assumption is adopted in the current work and will be validated in §3.

2.4. PSE solution procedure

Initial conditions for the PSE are obtained from linear stability solutions. Typically, these solutions are only easily obtained for the first few frequency modes (e.g. $m \leq 2$) that are linearly unstable. However, it is often necessary to introduce linearly stable,

high-frequency or high- β -wavenumber modes during the simulation, when the Fourier spectrum broadens. Initial conditions for these modes are obtained from an explicit solution for $\hat{\Phi}_{mn}$ according to the PSE governing equation

$$\mathcal{L}_{mn}^*(\hat{\Phi}_{mn}) = \mathbf{F}_{mn}, \tag{2.27}$$

where the streamwise derivative terms in \mathcal{L}_{mn} are removed to yield \mathcal{L}_{mn}^* . In order to generate a reasonable solution, the real part of α_{mn} is initially phase locked such that $\Re\{\alpha_{mn}\} = m\Re\{\alpha_{10}\}$, while the imaginary part of α_{mn} is set slightly negative (10^{-4}) to avoid numerical singularities. The frequency and spanwise wavenumber are fixed at their appropriate harmonic levels, $\omega_{mn} = m\omega_{10}$ and $\beta_{mn} = n\beta_{01}$. The result of this procedure is normalized according to the same method applied to the linear stability input functions: the maximum magnitude is set to unity and the phase is set such that \hat{v}_{mn} is purely real along the centreline.

Previous PSE studies have demonstrated that homogeneous Dirichlet boundary conditions in the free stream are adequate for accurate simulations (Herbert 1994). This approach, reasoned from the characteristic exponential decay of disturbances in the free stream, allows the approximation

$$\hat{\phi} = 0 \quad \text{as } y \rightarrow -\infty \quad \text{and } y \rightarrow \infty \tag{2.28}$$

to be applied without adverse effect, provided the boundary equation is applied far—at least $10\delta_\omega$ —from the centreline. However, applying the PSE to supersonic-shear-layer calculations often requires the solution of cases where a disturbance travels supersonically relative to either, or both, free streams. The oscillatory free-stream decay of these supersonic modes necessitates the use of an implicit boundary condition

$$\frac{\hat{\phi}'}{\hat{\phi}} = \mp q \quad \text{for } y \rightarrow \pm\infty, \tag{2.29}$$

where q is the coefficient of exponential decay obtained from the linear stability equations (Day 1999). The choice of boundary conditions is dependent on the modal phase speed, $c_r = \text{Re}(\omega/\alpha)$:

$$y \rightarrow -\infty : \begin{cases} \hat{\phi} = 0 & \text{for } c_r < c_- \\ \frac{\hat{\phi}'}{\hat{\phi}} = q & \text{for } c_r > c_-, \end{cases} \tag{2.30}$$

$$y \rightarrow \infty : \begin{cases} \hat{\phi} = 0 & \text{for } c_r > c_+ \\ \frac{\hat{\phi}'}{\hat{\phi}} = -q & \text{for } c_r < c_+, \end{cases} \tag{2.31}$$

where c_+ and c_- are the speed of sound of the fast and slow stream, respectively (Jackson & Grosch 1989).

Boundary conditions for the mean flow correction mode, $\hat{\phi}_{00}$, are treated slightly differently to allow for a non-zero \hat{v}_{00} at the boundary, which is necessary to satisfy mass-balance constraints as the mixing layer mean profile, $\bar{u} + \hat{u}_{00}\mathcal{A}_{00}$, grows downstream. As with the other modes, a mixed boundary condition is used: for supersonic flows the wave-based condition of equation (2.29) is employed, while subsonic flows are solved with the more commonly used combination of Neumann conditions for \hat{v}_{00} and Dirichlet conditions for the remaining variables.

The solution procedure of equation (2.20) requires discretization in both the streamwise and cross-stream directions. A fourth-order central difference approximation is

used in the latter, in combination with grid stretching to provide DNS-like resolution in y . In the streamwise direction, however, we note that the PSE method is constructed around the assumption of slow shape-function variation, and hence a first-order backward difference is sufficient. Recasting equation (2.20) as

$$\mathcal{L}_{mn}\hat{\phi}_{mn} = L_{mn}\hat{\phi}_{mn} + M_{mn}\frac{\partial\hat{\phi}_{mn}}{\partial x} = \frac{\hat{F}_{mn}}{\mathcal{A}_{mn}}, \quad (2.32)$$

the backward difference takes the form

$$[\Delta x L_{mn}^{i+1} + M_{mn}^{i+1}]\hat{\phi}_{mn}^{i+1} = M_{mn}^{i+1}\hat{\phi}_{mn}^i + \frac{\hat{F}_{mn}^{i+1}}{\mathcal{A}_{mn}^{i+1}}\Delta x. \quad (2.33)$$

The linear PSE solution is obtained by setting \hat{F}_{mn}^{i+1} to zero.

A cost-function approach based on the specified norm of equation (2.25) can be developed to yield the following iteration strategy for the wavenumber at each new streamwise step, α_{i+1} :

$$\alpha_{i+1}^{n+1} = \alpha_{i+1}^n - \frac{i}{\Delta x_i} \frac{\int_{\mathfrak{G}} (\hat{\mathbf{v}}_{i+1}^n)^\dagger (\hat{\mathbf{v}}_{i+1}^n - \hat{\mathbf{v}}_i^n) dy}{\int_{\mathfrak{G}} |\hat{\mathbf{v}}_{i+1}^n|^2 dy}, \quad (2.34)$$

where n indicates the iteration step number, $\hat{\mathbf{v}}$ is the vector of velocity shape functions, and \dagger denotes complex conjugate. At each iteration step, equation (2.33) is simultaneously solved for all stability modes, and iteration continues until the norm is globally satisfied to within 10^{-6} . As this procedure is carried downstream in a stepwise fashion, the nonlinear interactions will continue to grow until the iteration eventually fails to converge.

Typically, the convergence will stall and, in subsequent iterations, the shape functions will develop jagged profiles that are clearly non-physical. This development is particularly prone to occur in conditions of significant heat release where the mean temperature profile, by virtue of the infinitely fast-chemistry assumption, has a sharp discontinuity in its derivative. Indeed, this effect was the motivation behind including cross-stream viscous and heat conduction terms that naturally help to suppress this evolution. However, these terms will eventually be overwhelmed, resulting in diverging iterations which lead to overflow. In closing, it is noted that this failure is not too restrictive because it generally occurs just prior to the flow becoming highly nonlinear, at which point the PSE assumptions and hence their solutions are clearly invalid.

3. Central mode simulations

3.1. Validation

With the creation of any nonlinear model such as this implementation of the PSE technique, there is an obvious need for validation. Here we compare PSE and direct numerical simulation (DNS) results for a spatially developing mixing layer. Details of the DNS implementation are provided in Day (1999). Test conditions were selected to achieve a moderate compressibility while maintaining a two-dimensional, central-mode instability: $M_c = 0.5$, $\Theta = 0$, $r = 0.6$ and $s = 1$. A spatial DNS was calculated at $Re_o = 5000$ for these flow conditions in a computational box that spanned $(160 \times 30) \delta_{\omega_o}$. The complementary PSE solution was computed with eight frequency modes. Initial conditions for both simulations involved linear stability solutions of

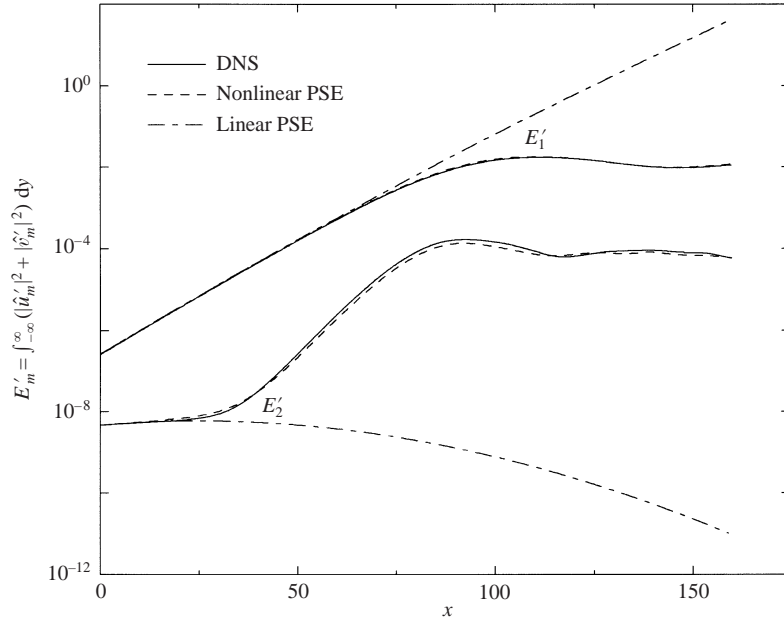


FIGURE 4. Comparison of DNS to linear and nonlinear PSE integrated energy results for the fundamental and first harmonic modes ($M_c = 0.5$, $r = 0.6$, $s = 1$, $\Theta = 0$, $M = 8$).

the fundamental and first modes harmonic forced at initial magnitudes of 0.001 and 0.0002, respectively. Forcing of the subharmonic mode to promote pairing will be discussed in the following section; initially, there was some question as to the ability of the parabolized equations to correctly model pairing so subharmonic forcing was avoided while validating the basic technique.

The first validation task is to look at the growth of individual modes from the initial condition through the linear and nonlinear stages. This is best done through an integrated measure like the modal energy,

$$E'_m \equiv \int_{-\infty}^{\infty} (|\hat{u}'_m|^2 + |\hat{v}'_m|^2 + |\hat{w}'_m|^2) dy, \quad (3.1)$$

where, for example, \hat{u}'_m is the time Fourier transform coefficient of the u velocity component at the frequency $\omega_m = m\omega_1$. This is related to the PSE shape function through $\hat{u}'_m = \hat{u}_m \cdot \mathcal{A}_m(x)$. Integrated energy results are shown in figure 4 for the first two modes of the DNS and PSE simulations, where the latter are shown for both linear and nonlinear calculations. For the fundamental mode ($m = 1$), excellent agreement between all solutions in the linear domain is followed by the departure of linear and nonlinear solutions at the start of saturation ($x \approx 75$). The linear solution, which lacks any such limit mechanism, continues its exponential growth. Figure 4 shows that the post-saturation result for the nonlinear PSE is indistinguishable from the DNS solution. Equally impressive agreement is found in the first harmonic ($m = 2$) mode. Starting at $x \approx 25$, the nonlinear PSE solution for this mode correctly models both the growth due to addition of energy from the fundamental mode and the eventual saturation. The difference between linear and nonlinear PSE solutions is particularly striking because this mode becomes stable without nonlinear interaction.

The energy growth of higher harmonics ($m = 3, 4$) of the PSE is shown in figure 5. The interest in these modes concerns their growth from the initial condition which

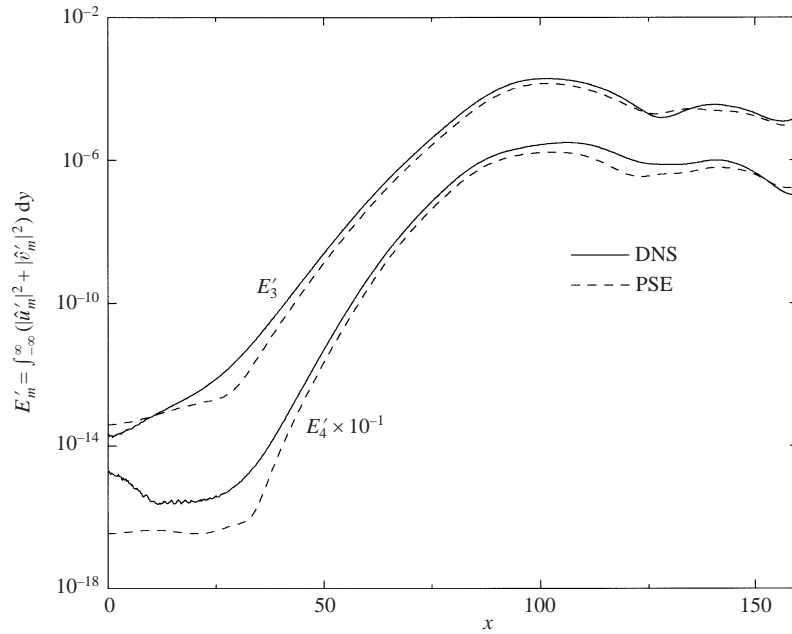


FIGURE 5. Comparison of DNS and PSE integrated energy results for two of the higher harmonics ($M_c = 0.5$, $r = 0.6$, $s = 1$, $\Theta = 0$, $M = 8$). Note that E'_4 results are shifted for readability.

was generated through equation (2.27) rather than with linear stability modes. The results demonstrate some disagreement early in the simulation when the energy level in these modes is low, but the comparison becomes excellent when the modes begin to play a role in the simulation by receiving energy via the cascade from lower, more dominant frequencies. The energy level in these modes also saturates later in the simulation, with the PSE solution predicting a slightly lower energy level than the DNS in the post-saturation phase.

Turning our attention now to the real-space flow field and related statistics, figure 6 compares DNS and PSE results for the streamwise evolution of the maximum velocity fluctuations in the u - and v -components. The agreement is again excellent. For \tilde{u}_{\max} the agreement between peak values is within 0.6% and the difference between the solutions is only discernible at the very late stages of the calculation. The results for \tilde{v}_{\max} are still impressive – the estimates of the peak differ by only 2.2% – although the level of the peak fluctuation intensity, at 14% of the mean value, suggests the presence of strong nonlinear effects where the PSE assumptions are not expected to hold.

A full-field appreciation for the PSE solution can be seen in the spanwise vorticity contour plots of figure 7. This streamwise evolution documents the nonlinear development of the central-mode flow structure. Agreement between nonlinear PSE and DNS calculations in figures 7(a) and 7(b) for the large-scale structure is excellent. A plot of the linear PSE contours in figure 7(c) offers an additional perspective on the importance of nonlinear modelling past $x = 65$, and clearly demonstrates why a nonlinear analysis is required to study the large-scale flow structure responsible for initiating mixing. The principal disagreement between the DNS and nonlinear PSE simulations concerns the small-scale structure which is a direct result of resolution problems when only eight frequency modes are tracked. An explicit demonstration of this is shown in

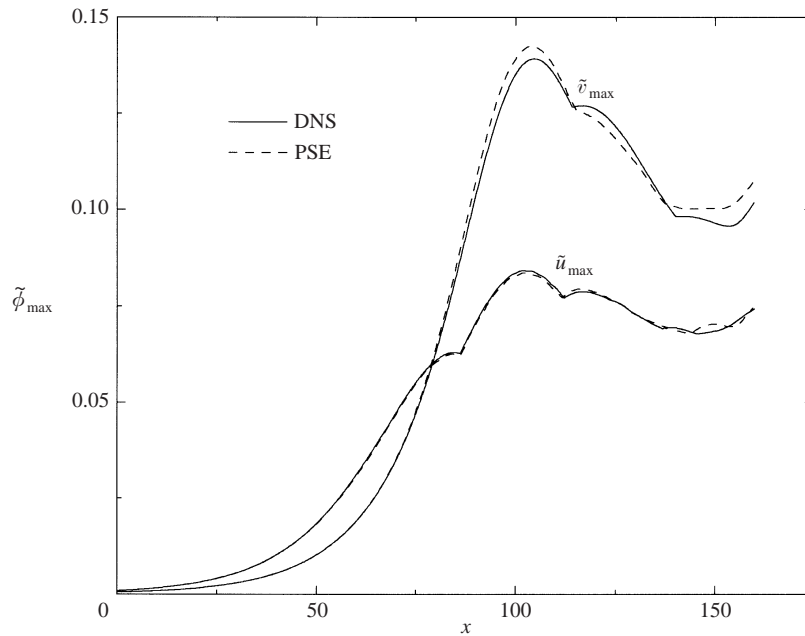


FIGURE 6. Comparison of PSE and DNS results for the maximum u and v fluctuation at a given streamwise position ($M_c = 0.5$, $r = 0.6$, $s = 1$, $\Theta = 0$, $M = 8$). Note that the kinks—present in both DNS and PSE calculations—are caused by the change in location of the maximum fluctuation.

figure 8(a), which plots a test function along with its representation using only eight Fourier modes. The truncated series simply lacks the spatial resolution to map the rapidly changing features of the test function. Oscillations result when the energy of the highest-resolved mode is not cancelled out by absent higher-order modes. Exactly the same phenomenon is seen in figure 8(b), where we plot the spanwise vorticity along the centreline from DNS and PSE calculations. Resolution problems result when a mode-truncated PSE simulation attempts to reproduce sharp gradients in the braid region. Truncation of the mode expansion in the PSE is responsible for the fine-scale fluctuations detected in the contours of figure 7(b). Accordingly, the reader is cautioned against attributing the fine-scale structure in contour plots to well-resolved, physical phenomenon.

With the fidelity of the PSE verified, the run time comparison becomes the critical result: the PSE calculation took fifteen minutes on a conventional workstation, roughly 350 times faster than the DNS calculation. Based on experience, it seems reasonable to characterize the increase in speed as $\approx 10^3$ and $\approx 10^4$ for two- and three-dimensional simulations, respectively. These numbers will reduce slightly when temporal rather than spatial DNS are used in the comparison. However, we note that temporal simulations, while statistically very useful, do not allow certain aspects like acoustics or asymmetry in the velocity profile to be studied.

3.2. Simulation of vortex pairing

The pairing of vortices is the dominant growth mechanism for the central mode (Winant & Browand 1974) and it is therefore essential that simulation techniques, regardless of their approximation, are able to capture this physics. This presents a significant challenge: by construction, parabolic methods exclude upstream propa-

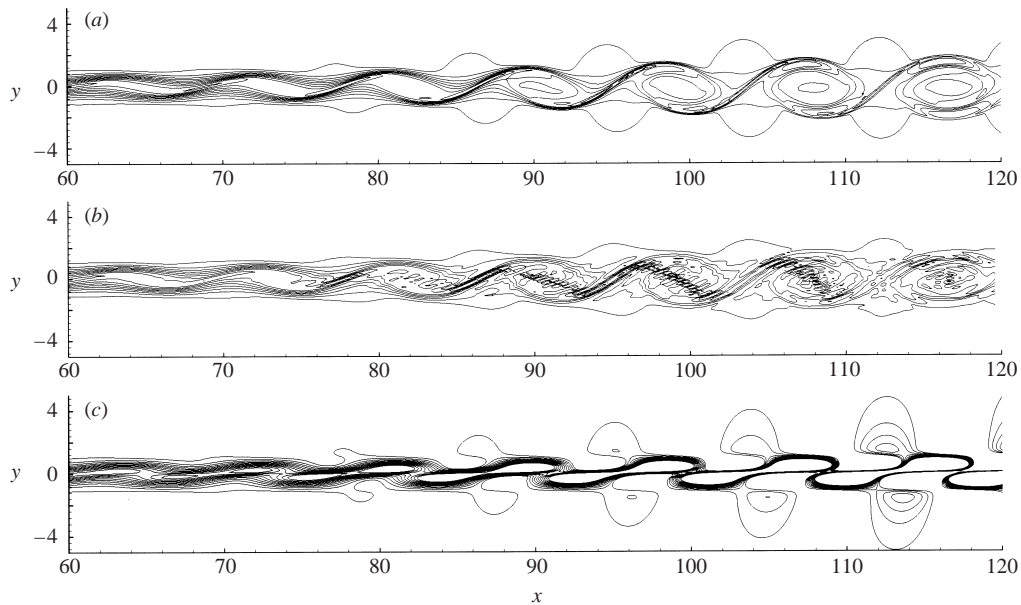


FIGURE 7. Comparison of spanwise vorticity contours for the test case ($M_c = 0.5$, $r = 0.6$, $s = 1$, $\Theta = 0$) with the contour max and min set to -0.42 and -0.02 and $\Delta\omega_z = 0.04$. Results are plotted for (a) DNS, (b) nonlinear PSE with $M = 8$, and (c) linear PSE.

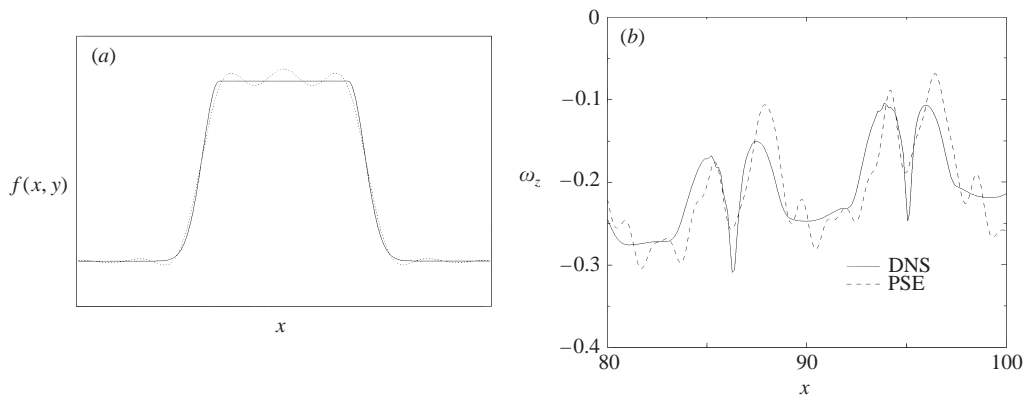


FIGURE 8. The effect on Fourier mode truncation on (a) a test function realized with both an infinite number and eight frequency modes and (b) the centreline ($y = 0$) spanwise vorticity for the conditions of figure 7.

gation of information, and this seems at odds with one explanation for vortex pairing based on interaction between vortices—their coupling and induced co-rotation—that implies an elliptic effect. However, modelling efforts by Monkewitz (1988) suggest that pairing is more simply related to the growth of instability waves. From this kinematic viewpoint, pairing is the result of the subharmonic mode ‘overtaking’ the fundamental instability without a significant interaction between the two. Further, the demonstrated importance of the phase difference in determining the choice between and efficiency of pairing and shredding (Monkewitz 1988; Hajj, Miksad & Powers 1993) suggests more support for a kinematic explanation than a Biot-Savart-type interaction. As Monkewitz points out, establishing a relation between instability

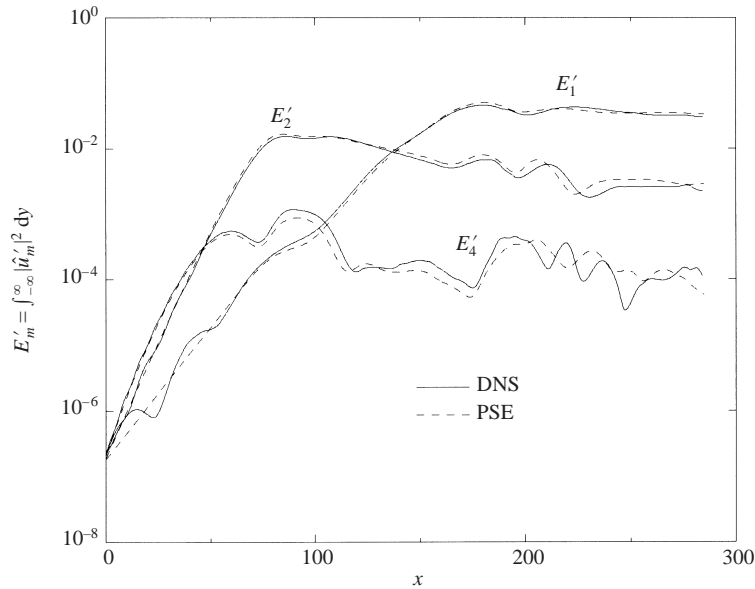


FIGURE 9. Comparison of \hat{u} energy between the DNS of Colonius *et al.* (1997) and PSE simulation results for the fundamental ($m = 4$), first subharmonic ($m = 2$), and second subharmonic ($m = 1$) modes ($M_c = 0.125$, $r = 0.5$, $s = 1$, $\Theta = 0$).

growth rates and a fundamental mechanism for shear-layer growth also provides insight on how *linear* stability theory (LST) can provide such an accurate prediction of experimentally observed flow phenomenon.

The PSE method offers an interesting tool to investigate this further by comparison to the DNS of Colonius, Lele & Moin (1997) at $Re = 5000$, $M_c = 0.125$, $s = 1$ and $r = 0.5$. Their spatial simulation, which was conducted to evaluate the accuracy of acoustic analogies, used an input velocity profile from the thin-shear-layer equations coupled with the most amplified (fundamental) linear instability disturbance and its first three subharmonics at the initial conditions, all with a normalized inlet magnitude of 0.001. A PSE simulation was constructed in a nearly identical manner, using a total of sixteen frequency modes to model the fundamental and first two subharmonics. In this configuration, the fundamental mode corresponds to $m = 4$ and the first and second subharmonics to $m = 2$ and $m = 1$, respectively.

A quantitative comparison of the two simulations is shown in figure 9, where integrated energy in \hat{u} for the three input modes is plotted. The PSE results for the subharmonic modes ($m = 1$ and 2) are nearly indistinguishable from the DNS solution at the streamwise positions where the mode is dominant. The agreement in the fundamental mode ($m = 4$) is also impressive but is not without some discrepancy in the later stages, which is most likely due to the mode truncation discussed earlier. A direct, visual comparison between results from DNS and PSE calculations can be made in the spanwise vorticity contour plots of figures 10(a) and 10(b). The qualitative agreement is excellent considering the mode-truncated nature of the PSE calculation. The large-scale features are nearly identical, with the location of the two vortex pairing events occurring at the same streamwise position. The close agreement demonstrates that the PSE have not eliminated the important physics, despite the approximation made in equation (2.26). This observation motivated a further simulation to investigate the degree of interaction between the modes by

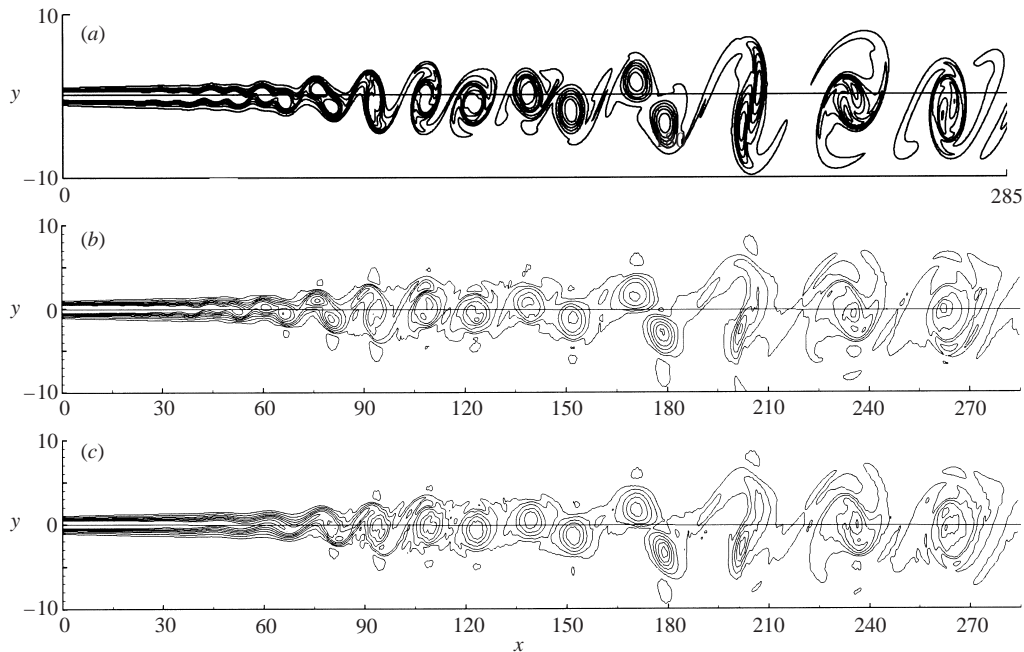


FIGURE 10. Comparison of spanwise vorticity contours for (a) DNS of Colonius *et al.* (1997), (b) the completely specified PSE, and (c) PSE simulation initialized without the fundamental mode ($M_c = 0.125$, $r = 0.5$, $s = 1$, $\Theta = 0$). Contour levels are set with $\Delta\omega_z = 0.04$, $\omega_{z\min} = -0.26$, and $\omega_{z\max} = 0.02$. The normal axis is expanded by a factor of 2.5; all images are plotted to the same scale.

removing the forcing of the fundamental. Spanwise vorticity contours for this case appear in figure 10(c). Comparison with figure 10(b) reveals that the only missing features are the vortices of the fundamental modes that first appear around $x = 60$; all other large-scale features – even early in the flow development – are nearly identical. The energy development for this case, not shown here (see Day 1999), also reveals little difference between the two remaining modes. The only observable change is a slightly earlier saturation in the first subharmonic ($m = 2$).

The close agreement between these plots suggests, in support of Monkewitz (1988), that the growth of stability modes is the controlling mechanism and that mutual pairing interactions play only a secondary role. However, the relative importance of mutual induction (Biot-Savart) between vortices cannot be established without a detailed analysis that lies beyond the scope of this investigation. But, regardless of the exact mechanism, these observations unequivocally show that the overall development of the layer through vortex pairing is closely connected to instability-mode growth rates. Indeed, as Monkewitz points out, this observation may provide a physical explanation for the accuracy of linear stability calculations. Winant & Browand (1974) demonstrated that the rate of pairing interactions determines the spreading rate of mixing layers, and hence LST, which accurately models the appropriate physics of the pairing process (the growth rate of instability waves), should also closely predict experimentally observed spreading rates. Some agreement with this hypothesis can be found in the suggestion of Hermanson & Dimotakis (1989) that the mechanism for vortex amalgamation (e.g. pairing) is inhibited by heat release.

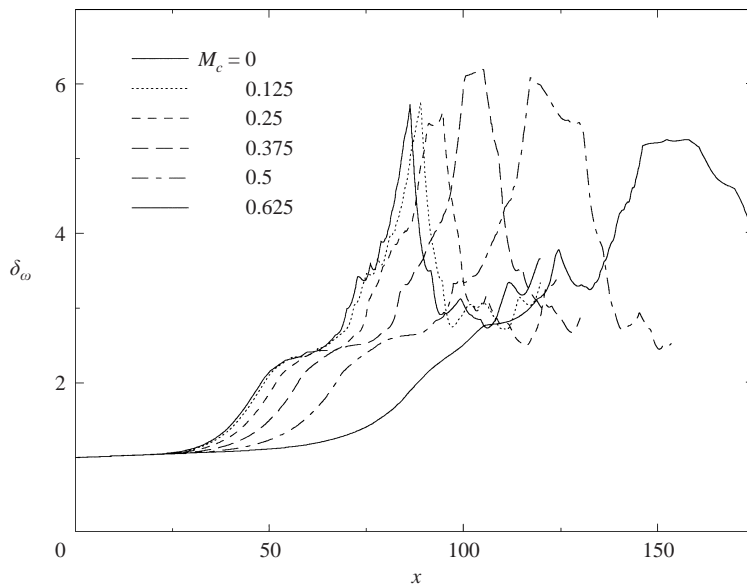


FIGURE 11. Effect of compressibility on the onset of pairing as visualized in the development of the vorticity thickness profile for two-dimensional PSE simulations ($r = 0.5$, $s = 1$, $\Theta = 0$, $Re = 5000$, $M = 8$).

This same effect is noted in LST growth-rate predictions (Shin & Ferziger 1993; Day *et al.* 1998).

Further support for this idea can be found by using the PSE to compare the effect of compressibility on LST growth rates and pairing distance. Six simulations, equally spaced between $M_c = 0$ and $M_c = 0.625$, were conducted with the two-dimensional PSE using eight frequency modes for otherwise identical input conditions ($r = 0.5$, $s = 1$, $Re = 5000$). The vorticity thickness evolution for these simulations is shown in figure 11. The delay in pairing, as measured by the increasing streamwise location of maximum vorticity thickness, is clearly seen with increasing compressibility. A direct comparison of this delay to the growth rate suppression of the most-amplified (i.e. fundamental) mode from linear stability calculations is shown in figure 12. The linear stability growth rate and pairing distance, the latter for both PSE and DNS results (for details, see Day 1999), have both been normalized by their values at $M_c = 0$. Plotted in this manner, the direct relationship between the two effects speculated by Sandham (1994) becomes clear. Here, the attenuation of instability waves with compressibility, which impacts both linear and nonlinear processes equally (Vreman *et al.* 1996), can be seen to directly account for the delay in vortex pairing.

4. Flow-structure mixing investigations

With the mixing layer validation now complete, our attention returns to the subject of reacting flows and, in particular, to mixing. This section begins with an investigation of central-mode mixing which provides a reference point for the outer-mode results to follow. We mention from the outset that the PSE can only be used as a first-order model of mixing. PSE assumptions inherently limit our resolution to only the first step in the combustion process: the entrainment of fluid that is governed by large-scale structure. The two subsequent steps of molecular mixing and chemical reaction

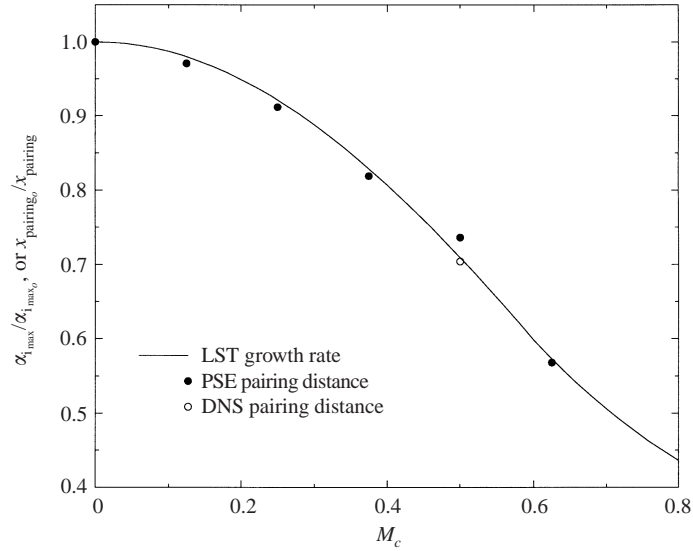


FIGURE 12. Comparison of the compressibility effect on the extension of pairing length and the suppression of the LST growth rate, both normalized on the incompressible result ($r = 0.5$, $s = 1$, $\Theta = 0$, $Re = 5000$, $M = 8$).

are either ignored, in the case of molecular mixing, or simplified, in the case of the fast-chemistry assumption for chemical reaction. It should be noted that finite-rate chemistry is inconsistent with the time-periodic nature of the PSE formulation; an equilibrium approach is conceivable but was not pursued in the current work.

Limitations notwithstanding, there is value in making general comments on the change in mixture-fraction probability density function (PDF) between different flow conditions, particularly for regimes that have not been previously addressed by either experiment or computation. PDFs provide a compact description of the time- and spanwise-averaged mixture fraction, defined as

$$\xi = \frac{Y_f - Y_o/n + Y_{o,\infty}/n}{Y_{f,-\infty} + Y_{o,\infty}/n}. \quad (4.1)$$

PDFs indicate the probability of finding fluid of mixture fraction $\xi \pm \Delta\xi/2$ at a given streamwise and cross-stream position in the flow; as such it is subject to the normalization

$$\int_0^1 P(\xi, x, y) d\xi = 1. \quad (4.2)$$

4.1. Central-mode mixing

A considerable body of literature has been dedicated to investigating mixture fraction PDF shapes in incompressible non-reacting flows (see Karasso & Mungal 1996, for a summary of results and discussion). In practice, experimental measurements of mixture fraction PDFs in this regime have shown considerable variation in shape. The main disagreement concerns whether the PDF shape should follow ‘marching’ or ‘non-marching’ behaviour. Marching implies that the most probable value of the mixture fraction, ξ , is nearly identical to the mean value at each cross-stream location. A non-marching PDF has a shape that is largely invariant to position.

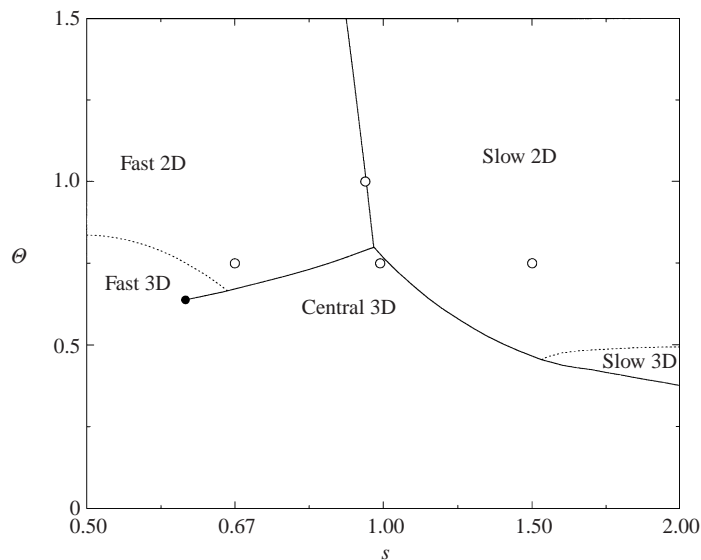


FIGURE 13. Plot of PSE cases on the mid-compressibility (s, Θ) regime chart of flow structure modes ($M_c = 1, \phi = 1.0, r = 0.5$). Case conditions are identified by \circ symbols; —, a boundary between distinct modes; ·····, a boundary between two- and three-dimensional structure for a particular mode.

Here, the presence of a preferred mixture-fraction value implies the dominance of large-scale structures. A ‘tilted’ profile describes an intermediate shape.

In compressible flows, experimental investigations by Dutton *et al.* (1990), Messersmith & Dutton (1992), Clemens & Mungal (1995) and Clemens & Paul (1995) are all in agreement that the mixture-fraction PDF displays a marching profile. However, Island (1997) notes that these results should be viewed cautiously because of resolution problems at the high Reynolds numbers of these experiments. In a well-resolved DNS of an annular shear layer, Freund (1997; see also Freund, Moin & Lele 1997) obtained a tilted PDF distribution at compressibility levels beyond the experimental conditions. However, instability modes were forced in this calculation, and the resulting large-scale structures bias the PDF toward a non-marching profile (Rogers & Moser 1994). Naturally, we expect to have the same bias in our PSE results because the method resolves only the large-scale flow structure.

Flow conditions for the four cases that will be discussed in this section are shown in the regime chart of figure 13, which plots the change in flow structure—both between dominant modes (solid lines) and two and three dimensions for a particular mode (dotted lines)—through a slice of the mixing layer’s parameter space. Full details on the construction of this regime chart are provided in Day *et al.* (1998). This study, in agreement with the results of Jackson & Grosch (1990), identifies heat release, compressibility and density ratio as the parameters of greatest import to the development of flow structure; velocity and equivalence ratio are secondary influences. As figure 13 demonstrates, the PSE mixing case conditions of the current investigation are selected by fixing compressibility and varying heat release and density ratio to generate the three different dominant flow structures and a fast/slow mode colayer case. Varying the compressibility is not essential to this study due to the similar effect of heat release and compressibility on flow structure (Jackson & Grosch 1990; Day *et al.* 1998).

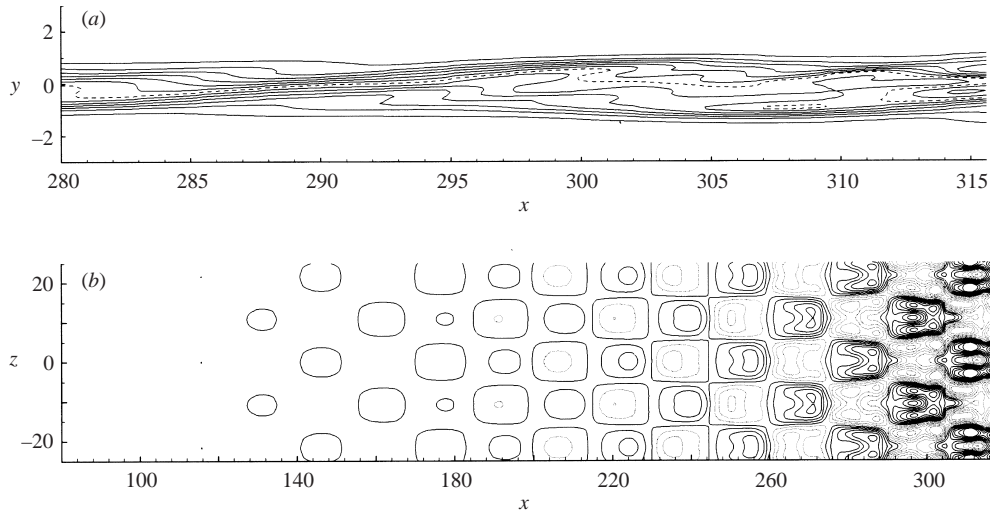


FIGURE 14. Mixture fraction field of the central mode in the (a) $z = 0$ and (b) $y = 0$ planes ($M_c = 1$, $\Theta = 0.75$, $\phi = 1$, $s = 1$, $r = 0.5$, $M = 5$, $N = 4$). Mixture fraction contours with $\Delta\xi = 0.08$, $\xi_{\max} = 0.98$, and $\xi_{\min} = 0.02$. Contours at the flame sheet location, $\xi = 0.5$, are dashed in (a) while all contours $\xi < 0.5$ are dotted in (b).

We begin discussion with the three-dimensional central-mode case of $M_c = 1$, $\Theta = 0.75$ and $s = 1$ that is simulated with $M = 5$ and $N = 4$. For all three-dimensional simulations of this section, input conditions consisted of forcing the (1,0) (fundamental) and (1,1) modes without phase shift at amplitudes of 0.001 and 0.0004, respectively. Further, all simulations are done at a Reynolds number of 10 000 and with $r = 0.5$ and $\phi = 1.0$. Figure 13 shows that this flow regime is very close to the transition boundary between central- and outer-mode flow regimes. A sense of the type of large-scale structure that results is given by figure 14. Plots of mixture fraction contours of the scalar field are shown in the cross-stream plane, $z = 0$ in figure 14(a) and in the spanwise plane, $y = 0$, in figure 14(b). The contours in the cross-stream plane of figure 14(a) do not show the roll-up of vorticity observed in non-reacting flows. This is a result of the significant heat release and compressibility which cause a shift away from the centrally dominant shape of the density-weighted mean vorticity profile, $\rho du/dy$ (see figure 1). The spanwise-plane view of figure 14(b) clearly shows strong three-dimensional features in this flow regime. We note that this calculation ends when the large energy content in multiple three-dimensional modes (i.e. the transition to turbulence) prohibits convergence of the PSE iteration at $x = 345$. Simulations of the three-dimensional central mode were the only calculations that were unable to run to saturation for this reason.

Probability density functions for the mixture-fraction field of this central-mode flow are shown in figure 15. Seven PDFs are shown at positions of equal spacing, $\Delta y = 1/8 \delta_{\text{vis}}$, between $y/\delta_{\text{vis}} = -3/8$ and $+3/8$. The probability distributions were constructed by sampling 400 times across the period of the fundamental mode and, at each time, 400 samples were taken across the largest spanwise wavelength. The results were distributed into 50 bins to yield $\Delta\xi = 0.02$. The bin corresponding to $\bar{\xi}$ at each position is shaded in on the figure to provide a reference point. We note that the lack of molecular-mixing effects causes step-function-like gradients at the bins corresponding to pure fluid. In a well-resolved computation these and other

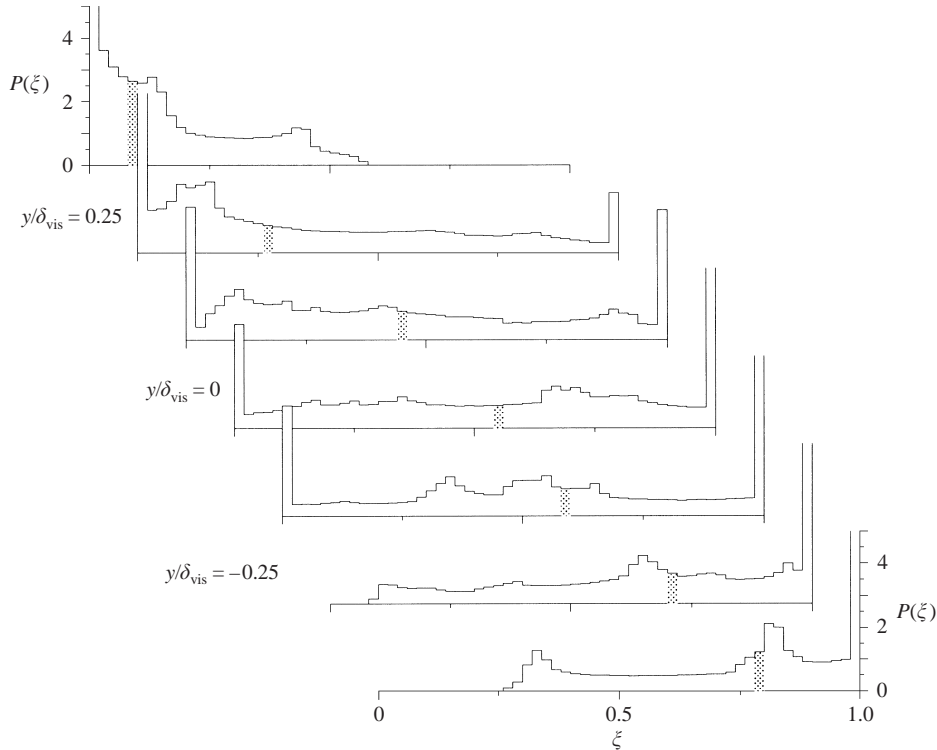


FIGURE 15. Mixture fraction PDFs at $x = 310$ and $z = 0$ for the central-mode flow of figure 14. Seven symmetric y -positions are represented with $\Delta y = 0.125\delta_{\text{vis}}$. The probability axis has been truncated for visualization purposes and the bin corresponding to $\bar{\xi}$ has been shaded in.

discontinuities in the PDF profiles would be smoothed out. However, the general shape of the profiles would remain unaltered and we will therefore restrict ourselves to comments of that nature. On this level, the principal measures of note in figure 15 are tilted PDFs. This feature is consistent with the observations of Freund (1997) in well-resolved direct numerical simulations of a compressible jet. Based on the results of Rogers & Moser (1994), we do not expect to obtain the marching PDFs viewed in compressible experiments because of our highly forced input condition (see Day 1999, for details). Further, the broad range of probability representation and the significant concentrations of pure fluid that exist (pure oxidizer at $\xi = 0$ and pure fuel at $\xi = 1$) at each cross-stream location is noted in figure 15. These latter observations are characteristic of the central-mode mixing mechanism schematically shown in figure 2(a): large-scale structures spanning the entire layer entrain fluid from both sides in a single-step process.

4.2. Single outer-mode mixing

The observations of the previous subsection are primarily of use as a basis of comparison to the outer-mode PDFs, which will now be discussed. The regime chart of figure 13 demonstrates that a 50% density bias in either free stream can result in an outer-mode-dominant flow structure at $M_c = 1.0$ and $\Theta = 0.75$, and these cases are discussed below. First, the mixture-fraction contours for the fast-mode case ($M_c = 1.0$, $\Theta = 0.75$, $\phi = 1$ and $s = 2/3$) are shown for both spanwise and streamwise cross-sections in figure 16. Contours in the spanwise plane demonstrate the largely

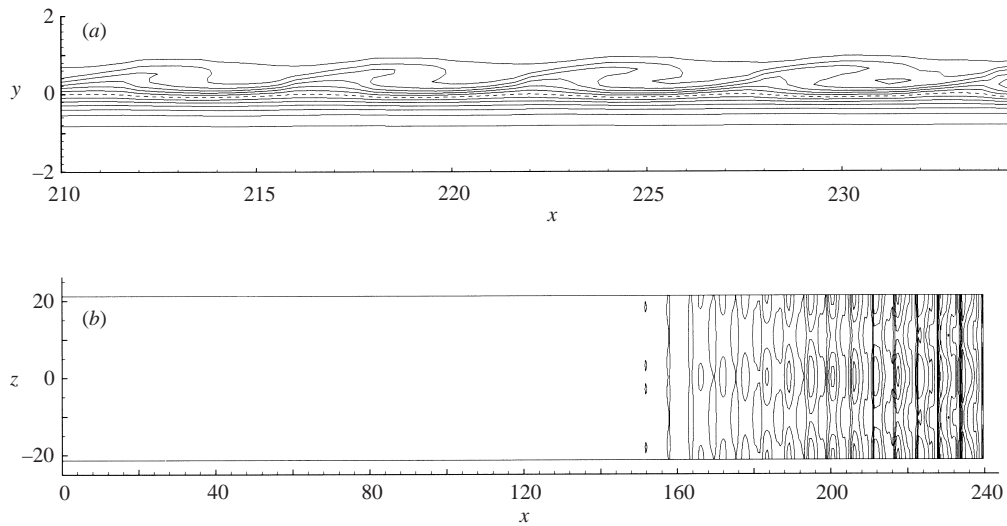


FIGURE 16. Mixture fraction field for a fast mode in compressible reacting conditions across (a) streamwise ($z = 0$) and (b) spanwise ($y = 0.5$) planes ($M_c = 1$, $\Theta = 0.75$, $\phi = 1$, $s = 2/3$, $r = 0.5$, $M = 5$, $N = 4$). Mixture fraction contours with $\Delta\xi = 0.08$, $\xi_{\max} = 0.98$, and $\xi_{\min} = 0.02$ and the flame sheet at $\xi = 0.5$ marked as a dotted line.

two-dimensional nature of the flow structure (Day *et al.* 1998). The streamwise view details the bias of the vortical structure towards one side of the layer, which severely limits mixing in the reacting zone and provides little convolution of the flame sheet (shown as the dotted contour).

This one-sided isolation is clearly seen in the PDF profiles plotted in figure 17 at $x = 230$, a streamwise position just past the saturation of the fast-mode fundamental instability. The lack of mixing on the slow side of the layer is evident in the near delta-function behaviour of the PDF for $y < 0$ positions. Even the centreline position displays only a modest range of mixture fraction values in comparison to what was seen with the central-mode case of figure 15. The majority of the mixing influence is, understandably, concentrated on the fast side, although even these PDFs demonstrate a fairly limited range of populated mixture fraction values. Each of these three fast-side PDF locations also feature a dominant probability of pure fluid. These distributions suggest a combustion process that is well supplied with oxidizer from mixing action on the fast side but is limited by the delivery of fuel through diffusion from the slow stream.

A similar set of plane views and PDF plots for flow structures that develop in the slow stream are shown in figures 18 and 19. Here, the larger growth rate of the slow mode results in fundamental-mode saturation at $x = 125$. Similar to the fast-mode case, the flow structure is largely two-dimensional, and exists entirely on one side of the flame sheet. A comparison of slow-mode PDFs to the fast-mode case indicates an even greater polarization to one side. The delta-function behaviour extends all the way to the centre of the layer, implying that no appreciable mixing action extends down to the flame sheet position. Instead, the mixing influence from the slow mode is only present at the three positions on the slow side of the layer. Each of these positions demonstrates a similar probability distribution, having a strong bias towards pure fuel concentrations and a range of populated bins that only extends to $\xi \approx 0.5$.

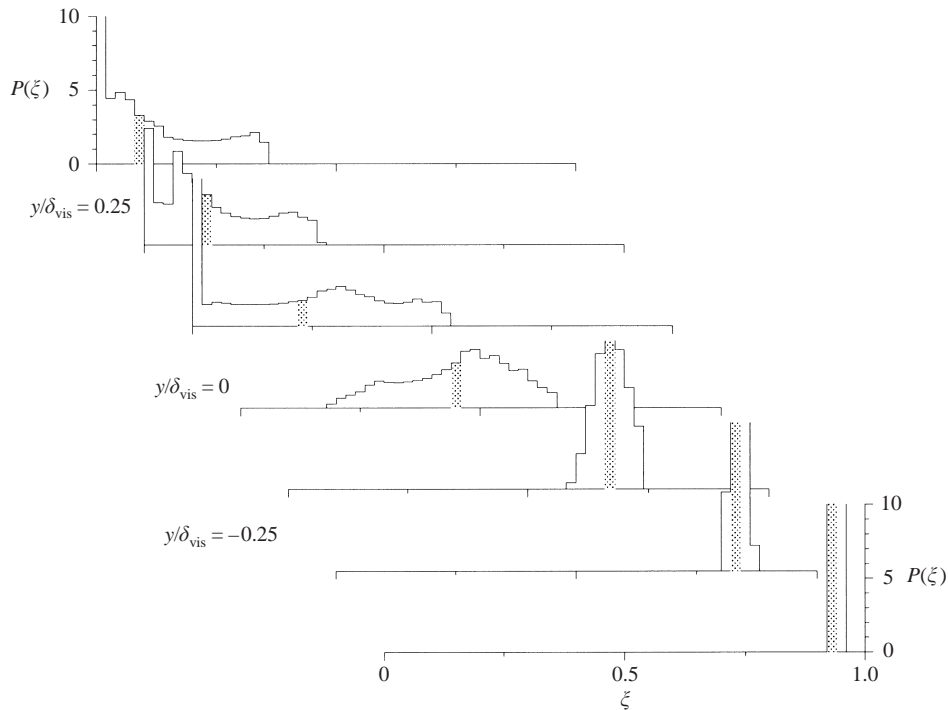


FIGURE 17. Mixture fraction PDF at $x = 230$ for the fast-mode flow of figure 16. Seven symmetric y -positions are represented with $\Delta y = 0.125\delta_{\text{vis}}$. The probability axis has been truncated for visualization purposes and the bin corresponding to $\bar{\xi}$ has been shaded in.

4.3. Colayer simulations and mixing

Results presented for single outer-mode flows motivate an investigation of colayers, a special case where two modes are equally amplified and an opportunity for mixing enhancement exists. A fast/slow colayer case was simulated for the conditions $M_c = 1$, $\Theta = 1$, $s = 0.94$, a point that lies directly on the regime boundary of figure 13. This chart also shows the two-dimensional dominance of the outer modes at these conditions and, correspondingly, a two-dimensional PSE simulation was first run. To investigate the long-term development of this flow structure, subharmonics of the fundamental modes were also forced at the inlet. More specifically, the fundamental fast and slow modes were forced at a magnitude of 0.001 and with frequencies $m = 6$ and $m = 4$. These frequencies were chosen to correspond to the most unstable frequencies determined by linear stability. The subharmonics were forced at $m = 2$ (slow) and $m = 3$ (fast) with half the magnitude of the fundamental and a phase shift of $\phi_s = \pi/2$ to optimize their interaction with the fundamental modes (Planché 1992). The second subharmonic of the slow mode was also introduced with negligible forcing at $m = 1$.

Energy development of the principal modes is shown in figure 20 with circles marking the points where energy in a subharmonic overtakes the fundamental mode. The colayer nature of the flow is evident in the similar (exponential) growth rates of the two fundamental modes; the slight difference results from forcing these instabilities at discrete frequencies prescribed by the PSE. Interestingly, the slow mode reaches saturation first at 50% of the fast-mode energy level. Both fundamentals decay in energy with further streamwise development and are eventually overtaken by

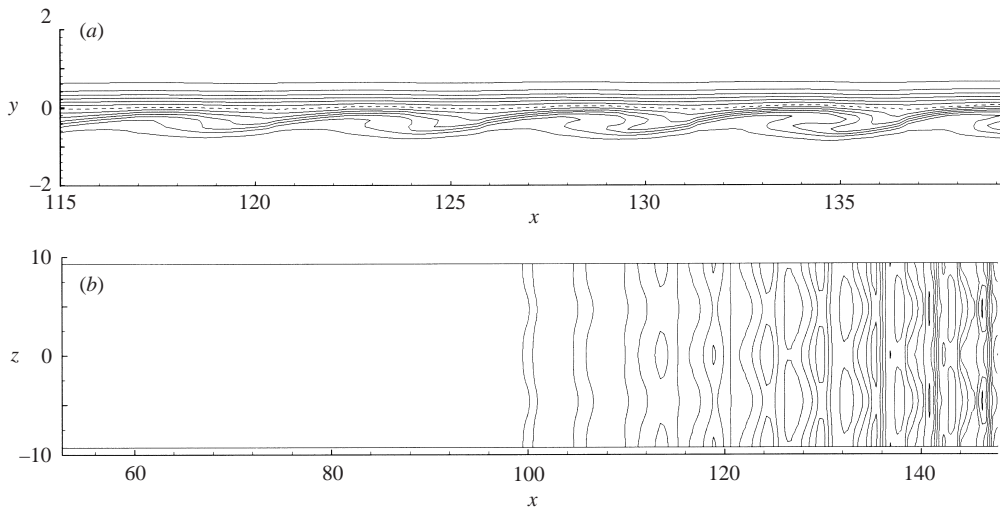


FIGURE 18. Mixture fraction field for a slow mode in compressible reacting conditions across (a) streamwise ($z = 0$) and (b) spanwise ($y = -0.58$) planes ($M_c = 1$, $\Theta = 0.75$, $\phi = 1$, $s = 3/2$, $r = 0.5$, $M = 5$, $N = 4$). Mixture fraction contours with $\Delta\xi = 0.08$, $\xi_{\max} = 0.98$, and $\xi_{\min} = 0.02$ and the flame sheet at $\xi = 0.5$ marked as a dotted line.

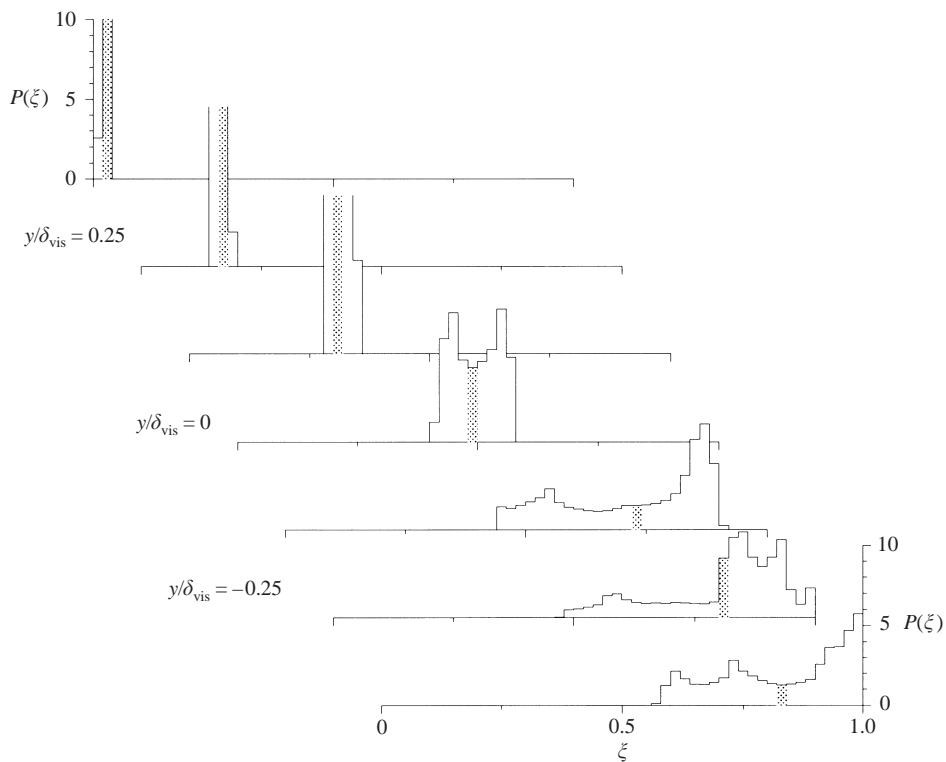


FIGURE 19. Mixture fraction PDF at $x = 140$ for the slow-mode flow of figure 18. Seven symmetric y -positions are represented with $\Delta y = 0.125\delta_{\text{vis}}$. The probability axis has been truncated for visualization purposes and the bin corresponding to $\bar{\xi}$ has been shaded in.

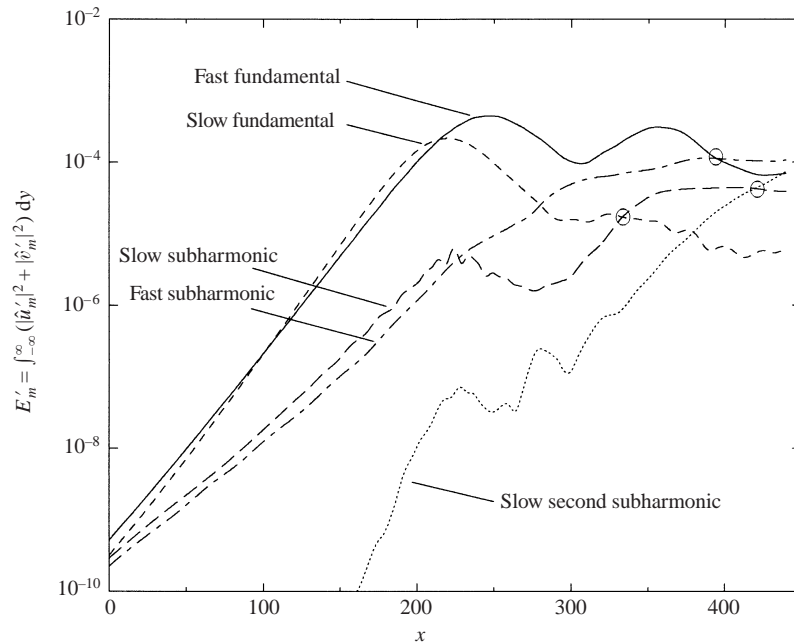


FIGURE 20. Energy evolution in a fast/slow mode colayer case with subharmonics of both the fast and slow modes initialized with $\phi_s = \pi/2$ ($M_c = 1$, $\Theta = 1$, $\phi = 1$, $s = 0.94$, $r = 0.5$, $M = 24$, $N = 0$). The \circ symbols denote a change in dominance from a higher to lower harmonic.

their subharmonics at $x = 330$ for the slow mode and $x = 395$ for the fast. The second subharmonic of the slow mode grows rapidly throughout the simulation and eventually overtakes the first subharmonic at $x = 420$.

Three views of the corresponding development in the mixture-fraction field are shown in figure 21. The earliest view in figure 21(a) corresponds to the first saturation point and the dominance of energy in the two fundamental modes results in clearly observable flow structure on both sides of the layer. This mixing field appears to be a superposition of two single-mode simulations: the vortical mixing is completely isolated to either side and the convolution of the flame sheet (the dotted line) is negligible, implying little mixing in the reaction zone. Indeed, this is the nature of the independent, two-step mixing process that was described in § 1 (see figure 2).

With longer streamwise development, the flow structure becomes convoluted by the competing influence of the fundamental and subharmonic modes, which are now at equal energy levels. Compared to the slow modes, the fast fundamental and subharmonic contain more energy and their combined presence has increased the thickness of the layer and, in the final view of figure 21, has pushed the flame sheet towards the slow side. However, this increase in thickness occurred without vortex pairing, in contrast to what is observed when a central mode is dominant (see § 3). DNS studies by Planché & Reynolds (1992) (and Planché 1992, in greater detail) observed the same phenomenon and termed it ‘gulping’. Analysis of vorticity generation terms in these DNS studies revealed the presence of a large baroclinic torque that acts to prevent outer-mode structures from pairing. They also identified the elongated shape and absence of roll-up in the outer-mode vortices as factors in producing the gulping behaviour.

The mixing characteristics of this flow were investigated with a three-dimensional

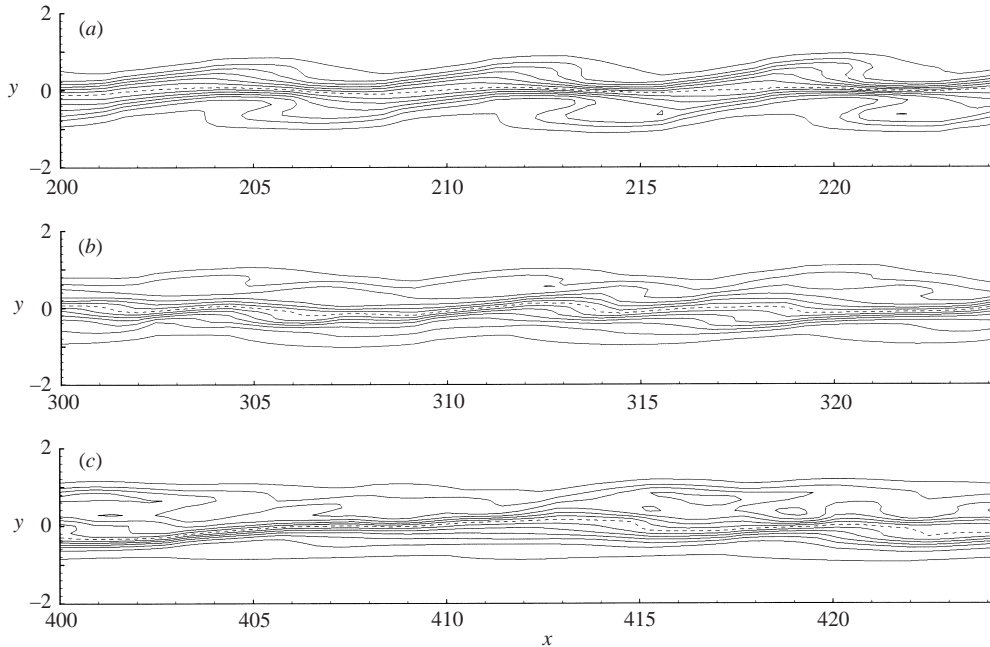


FIGURE 21. Evolution of the mixture fraction field for the fast/slow colayer of figure 20. Three visualizations are shown at x -locations where (a) the fundamental modes dominate ($x = 200$) and where a mode transition is taking place at (b) $x = 300$ and (c) $x = 400$. Mixture fraction contours with $\Delta\zeta = 0.08$, $\zeta_{\max} = 0.98$, and $\zeta_{\min} = 0.02$ and the flame sheet at $\zeta = 0.5$ marked as a dotted line.

PSE simulation of the same case, but without resolving the subharmonics. Three-dimensional simulations are required for PDF construction because they provide a second statistical dimension to the flow, which results in a far better realization of the PDF than sampling over the time period alone. Plots of the mixture fraction contours through the $z = 0$ plane are shown at three different times in figure 22 to detail the structure evolution. The plots are separated by $\Delta t = \pi$ where, for the special case of this simulation, the periods of the fast and slow modes are 2π and 4π . Dotted lines are drawn between plots to indicate the displacement in time of a specific fast- and slow-mode structure. The difference in slope between these lines is proportional to the phase-speed difference of the modes: 0.64 and 0.88 for the slow and fast fundamentals, respectively. The difference would be more significant if the velocity ratio were reduced, but $r = 0.5$ was set constant in all simulations.

The mixture fraction PDF of this flow structure at $x = 230$ is shown in figure 23 using the same plotting convention as the previous section. Similar to the mixture fraction field, the colayer PDF has the appearance of being constructed from half of each single-mode PDF sequence of figures 17 and 19. Again, this implies very little communication between the different sides. However, the presence of mixing on both sides of the layer, even without direct interaction, represents significant enhancement relative to the single-mode PDFs of the previous section. It is also noted that figure 23 is very similar to the PDFs from Planché's (1992) three-dimensional DNS simulations. Our PSE-based PDF at the centreline even replicates the probability bias towards the slow stream that was observed in Planché's DNS results. This was attributed to the better performance of the slow mode in entraining pure fluid to the reacting zone.

With the mixing enhancement of colayers now established, there is a need to

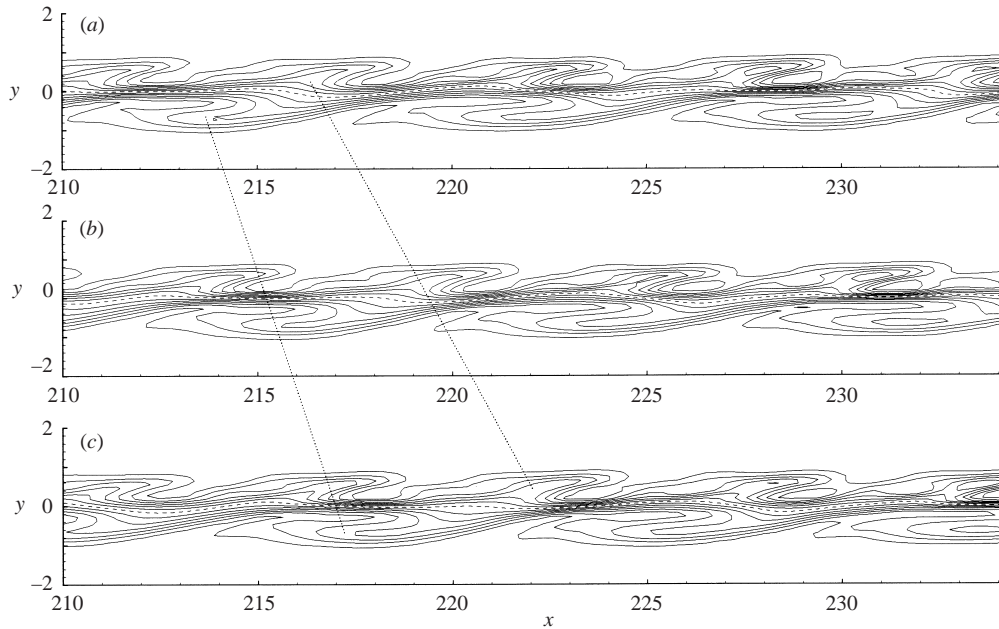


FIGURE 22. Mixture fraction field for a fast/slow colayer in compressible reacting conditions visualized at (a) $t = 0$, (b) $t = \pi$, and (c) $t = 2\pi$ ($M_c = 1$, $\Theta = 1$, $\phi = 1$, $s = 0.94$, $r = 0.5$, $M = 4$, $N = 4$). Mixture fraction contours with $\Delta\xi = 0.08$, $\xi_{\max} = 0.98$, and $\xi_{\min} = 0.02$ and the flame sheet at $\xi = 0.5$ marked as a dotted line. Lines joining plots indicate the streamwise movement of a fast and slow structure.

determine how common these conditions are in a real flow. Specifically, the question concerns the effective ‘thickness’ of the colayer lines that were plotted in the regime chart of figure 13: how close to those boundaries do the flow conditions need to be to observe colayers? Linear stability results suggest that the boundaries are very thin; a slight difference in exponential growth rates will eventually lead to the dominance of one mode over another. In reality, however, there is a saturation mechanism in place that limits this exponential growth. If saturation occurs before the difference in growth rates can effectively separate the modes, then colayer conditions will be observed in the resulting flow structure.

Several PSE simulations of a fast/slow colayer were conducted to determine the sensitivity of this dual-mode flow to changing conditions. Starting at a fast/slow colayer point, the density ratio was increased to move in a direction normal to the colayer boundary. The progression of these points on the (s, Θ) regime chart is shown in figure 24(a). The corresponding linear stability growth rates of the fast and slow modes appear in figure 24(b), which provides a further view of the strong effect the density ratio has on the relative amplification of the outer modes (Jackson & Grosch 1990; Day *et al.* 1998). A qualitative view of what this does to the flow structure is seen in the mixture-fraction contours of figure 25. The 30% change in density ratio between the first and last case is enough to apparently erase the fast-mode flow structure. The fast mode will eventually appear with further streamwise development, although probably only after the point that the slow mode has interacted with its subharmonics and grown appreciably in both size and energy. Our conclusion is that the range of fast/slow colayer conditions—and hence the mixing enhancement they provide—will be relatively limited in the mixing-layer parameter space.

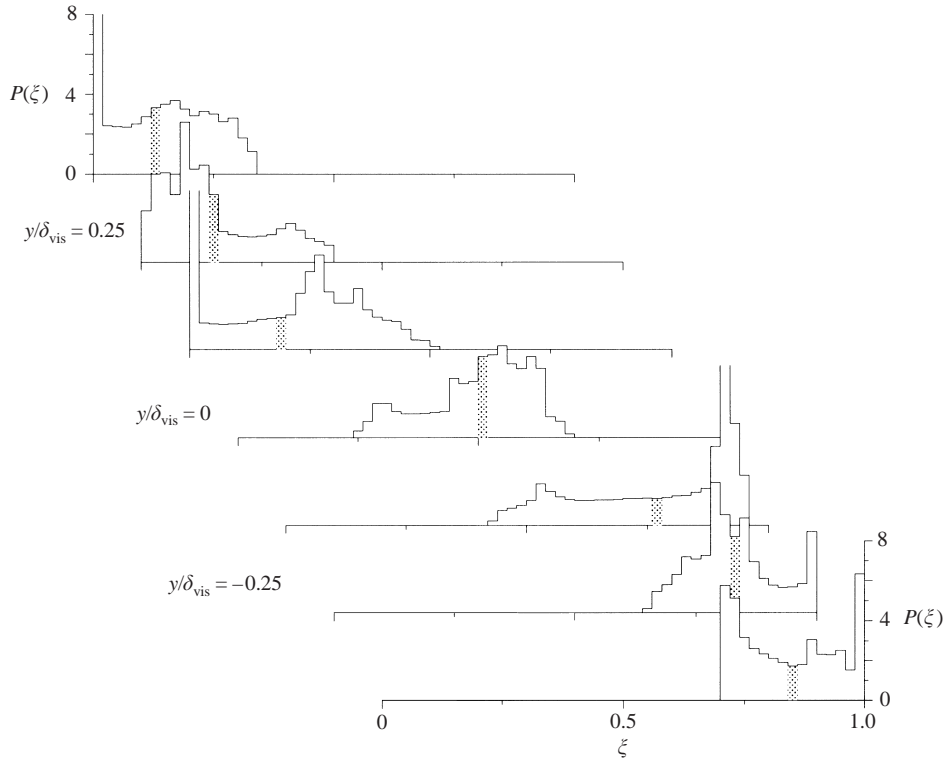


FIGURE 23. Mixture fraction PDF at $x = 230$ for the fast/slow colayer of figure 22. Seven symmetric y -positions are represented with $\Delta y = 0.125 \delta_{vis}$. The probability axis has been truncated for visualization purposes and the bin corresponding to $\bar{\xi}$ has been shaded in.

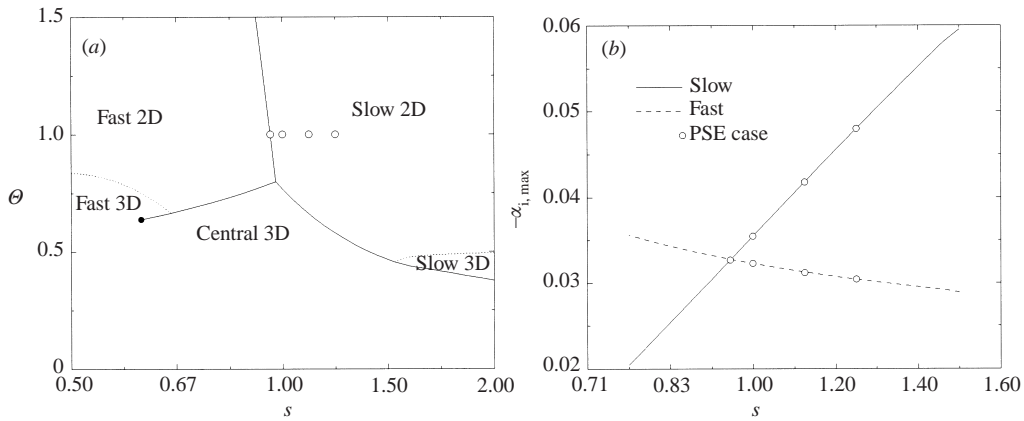


FIGURE 24. Location of colayer width test cases on (a) the (s, θ) regime chart and (b) LST growth rate plot with density ($M_c = 1$, $r = 0.5$, and $\phi = 1.0$; $\theta = 1$ in plot b). Case conditions are identified by \circ symbols.

5. Conclusions

The parabolized stability equations have been applied to the study of both reacting flows and mixing layers for the first time. A comprehensive and very favourable comparison of the technique to DNS results was provided for sub- and supersonic

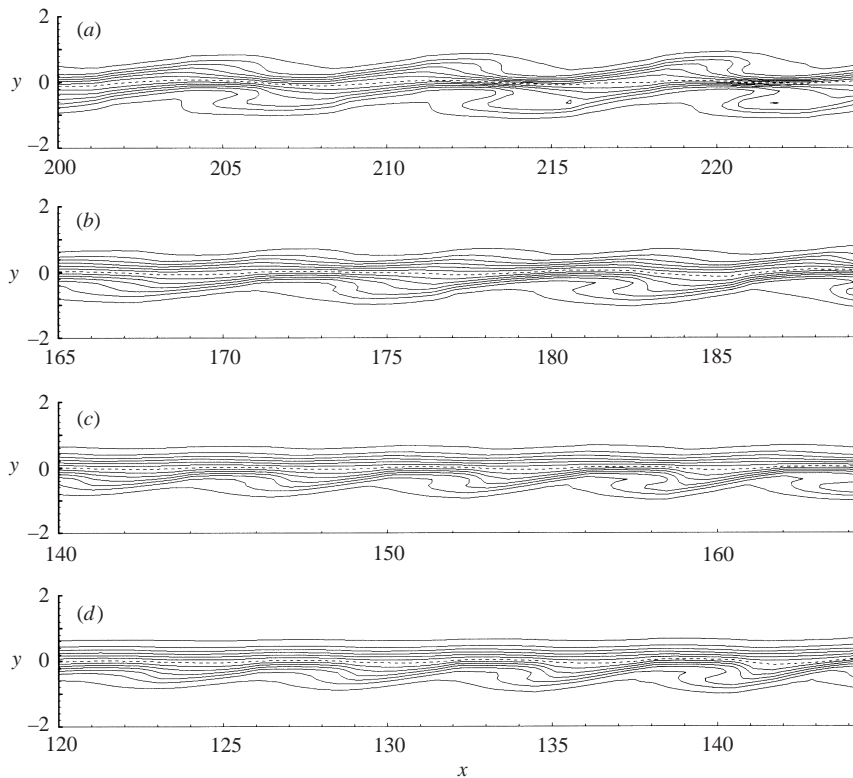


FIGURE 25. Evolution of the mixture fraction field for a colayer case with increasing slow side density bias: (a) $s = 0.94$ (colayer), (b) $s = 1.0$, (c) $s = 1.125$, and (d) $s = 1.25$ ($M_c = 1$, $\Theta = 1$, $r = 0.5$, $\phi = 1.0$, $M = 8$). Mixture fraction contours with $\Delta\xi = 0.08$, $\xi_{\max} = 0.98$, and $\xi_{\min} = 0.02$ and the flame sheet at $\xi = 0.5$ marked as a dotted line.

conditions, thereby validating the technique—and this implementation in particular—for the study of free-shear-layer flows. The ability of the PSE to accurately model vortex pairing was also demonstrated by comparison between PSE and DNS results. This capability was exploited to extend the conclusion of Monkewitz (1988) into the fully nonlinear, non-parallel domain: vortex pairing appears to be determined simply by the independent growth of instability waves. While our demonstrations cannot definitively exclude the mutual induction mechanism (Biot-Savart), they do suggest that induction is of secondary importance to the growth of stability modes in controlling vortex pairing. This observation received further support in the demonstration that the delay in pairing caused by compressibility was very closely correlated with the attenuation of instability growth rates. Thus, the accurate prediction of pairing—the mechanism responsible for nonlinear mixing layer growth—from linear growth rates offers insight into why linear stability theory is such an effective analysis technique for mixing layers.

This investigation has demonstrated the ability of the PSE to be useful in *qualitative* mixing studies using an infinitely fast-chemistry assumption. Central-mode mixture-fraction PDF distributions demonstrated the efficient nature of this mode's mixing mechanism through their large range of probability representation and the existence of both pure reactants in a significant span of cross-stream positions. This is in stark contrast to the mixture-fraction PDFs generated by outer-mode flow structure. Their

shape was relatively compact on the side associated with the mode, while the PDF approached the delta-function behaviour of laminar flow on the opposite side. This is a clear indication that the impact of the outer modes on mixing is entirely localized to one side, and is separated from the other by the flame sheet.

The nonlinear development of the fast/slow colayer was also studied. Subharmonics of the outer modes were found to overtake the fundamental without pairing. This process occurred without any interaction between the different sides of the layer. Mixture fraction PDFs indicated a similar lack of communication across the flame sheet. They appeared to have been formed by the superposition of two PDFs from flows where the outer modes appeared individually. While this colayer flow presents a significant enhancement of mixing relative to a single-outer-mode configuration, it does not approach the degree of mixing provided by the central mode. Further, nonlinear stability studies indicated that the width of fast/slow colayer conditions on the regime charts was, in practice, quite limited: a 25% change in density ratio relative to a colayer case resulted in complete dominance of flow structure on the density-biased side.

This work was sponsored by the Air Force Office of Scientific Research, the Natural Sciences and Engineering Research Council of Canada (in the form of support for M.J.D.), and the Center for Turbulence Research. The authors would also like to thank Dr Chris Hill for his useful insight into the PSE technique.

REFERENCES

- ANDERSSON, P., HENNINGSON, D. S. & HANIFI, A. 1998 On a stabilization procedure for the parabolic stability equations. *J. Engng Maths* **33**, 311–332.
- BERTOLOTTI, F. P., HERBERT, T. & SPALART, P. R. 1992 Linear and nonlinear stability of the Blasius boundary layer. *J. Fluid Mech.* **242**, 441–474.
- BOGDANOFF, D. W. 1983 Compressibility effects in turbulent shear layers. *AIAA J.* **21**, 926–927.
- BROWN, G. L. & ROSHKO, A. 1974 On density effects and large structure in turbulent mixing layers. *J. Fluid Mech.* **64**, 775–816.
- CHEN, L. D., SEABA, J. P., ROQUEMORE, W. M. & GOSS, L. P. 1988 Buoyant Diffusion Flames. In *Twenty-Second Symp. (Intl) on Combustion*, pp. 677–684. The Combustion Institute, Pittsburgh, USA.
- CHINZEL, N. G., MASUYA, T., KOMURO, T., MURAKAMI, A. & KUDOU, K. 1986 Spreading of two-stream supersonic turbulent mixing layers. *Phys. Fluids* **29**, 1345–1347.
- CLEMENS, N. T. & MUNGAL, M. G. 1995 Large-scale structure and entrainment in the supersonic mixing layer. *J. Fluid Mech.* **284**, 171–216.
- CLEMENS, N. T. & PAUL, P. H. 1995 Scalar measurements in compressible axisymmetric mixing layers. *Phys. Fluids* **7**, 1071–1081.
- COLONIUS, T., LELE, S. K. & MOIN, P. 1997 Sound generation in a mixing layer. *J. Fluid Mech.* **330**, 375–409.
- DAY, M. J. 1999 Structure and stability of compressible reacting mixing layers. PhD thesis, Stanford University, Stanford, CA 94305.
- DAY, M. J., MANSOUR, N. N. & REYNOLDS, W. C. 1999 Structure and stability of compressible reacting mixing layers. *Rep. TF-75*, Mechanical Engineering Department, Stanford University.
- DAY, M. J., MANSOUR, N. N. & REYNOLDS, W. C. 1998 The structure of the compressible reacting mixing layer: Insights from linear stability analysis. *Phys. Fluids* **10**, 993–1007.
- DUNN, D. W. & LIN, C. C. 1955 On the stability of the laminar boundary in a compressible fluid. *J. Aero. Sci.* **22**, 455–477.
- DUTTON, J. C., BURR, R. F., GOEBEL, S. G. & MESSERSMITH, N. L. 1990 Compressibility and mixing in turbulent free shear layers. In *Proc. 12th Symp. on Turbulence, Rolla, MO* (ed. X. B. Reed). University of Missouri.

- FREUND, J. B. 1997 Compressibility effects in a turbulent annular mixing layer. PhD thesis, Stanford University, Stanford, CA 94305.
- FREUND, J. B., MOIN, P. & LELE, S. K. 1997 Compressible effects in a turbulent annular mixing layer. *Rep. TF-72*, Mechanical Engineering Department, Stanford University.
- GROPENGIESSER, H. 1970 Study on the stability of boundary layers and compressible fluids. *Tech. Rep. TT F-12786*. NASA.
- HAJ-HARIRI, H. 1994 Characteristics analysis of the parabolized stability equations. *Stud. Appl. Maths* **92**, 41–53.
- HAJJ, M. R., MIKSAD, R. W. & POWERS, E. J. 1993 Fundamental-subharmonic interaction: effect of phase relation. *J. Fluid Mech.* **256**, 403–426.
- HALL, J. L. 1991 An experimental investigation of structure, mixing and combustion in compressible turbulent shear layers. PhD thesis, California Institute of Technology.
- HERBERT, T. 1994 Parabolized stability equations. *Tech. Rep. AGARD-FDP-VK1*. Special Course on Progress in Transition Modeling, AGARD-R-793. Von Kármán Inst., Rhode-Saint-Genese, Belgium.
- HERBERT, T. & BERTOLOTTI, F. P. 1987 Stability analysis of nonparallel boundary layers. *Bull. Am. Phys. Soc.* **32**, 2079.
- HERMANSON, J. C. & DIMOTAKIS, P. E. 1989 Effects of heat release in a turbulent, reacting shear layer. *J. Fluid Mech.* **199**, 333–375.
- HO, C.-M. & HUERRE, P. 1984 Perturbed free shear layers. *Ann. Rev. Fluid Mech.* **16**, 365–424.
- ISLAND, T. 1997 Quantitative scalar measurements and mixing enhancement in compressible shear layers. PhD thesis, Stanford University, Stanford, CA 94305; also available as *Rep. TSD-104*, Mechanical Engineering Department, Stanford University.
- JACKSON, T. L. & GROSCH, C. E. 1989 Inviscid spatial stability of a compressible mixing layer. *J. Fluid Mech.* **208**, 609–637.
- JACKSON, T. L. & GROSCH, C. E. 1990 Inviscid spatial stability of a compressible mixing layer. Part 2. The flame sheet model. *J. Fluid Mech.* **217**, 391–420.
- KARASSO, P. S. & MUNGAL, M. G. 1996 Scalar mixing and reaction in plane liquid shear layers. *J. Fluid Mech.* **323**, 23–63.
- KONRAD, J. H. 1976 An experimental investigation of mixing in two-dimensional turbulent shear flows with applications to diffusion-limited chemical reactions. PhD thesis, California Institute of Technology.
- KOCHESFAHANI, M. M. & DIMOTAKIS, P. E. 1986 Mixing and chemical reactions in a turbulent liquid mixing layer. *J. Fluid Mech.* **170**, 83–112.
- KUO, K. 1986 *Principles of Combustion*. John Wiley & Sons.
- LESSEN, M., FOX, J. A. & ZIEN, H. M. 1965 On the inviscid instability of the laminar mixing of two parallel streams of a compressible fluid. *J. Fluid Mech.* **23**, 355–367.
- LESSEN, M., FOX, J. A. & ZIEN, H. M. 1966 Stability of the laminar mixing of two parallel streams with respect to supersonic disturbances. *J. Fluid Mech.* **25**, 737–742.
- LI, F. & MALIK, M. R. 1996 On the nature of the PSE approximation. *Theor. Comput. Fluid Dyn.* **8** (5), 253–273.
- MASUTANI, S. M. & BOWMAN, C. T. 1986 The structure of a chemically reacting plane mixing layer. *J. Fluid Mech.* **172**, 93–126.
- MESSERSMITH, N. L. & DUTTON, J. C. 1992 An experimental investigation of organized structure and mixing in compressible turbulent free shear layers. *Tech. Rep. UILU-ENG 92-4002*. University of Illinois.
- MILLER, M. F., BOWMAN, C. & MUNGAL, M. 1998 An experimental investigation of the effects of compressibility on a turbulent reacting mixing layer. *J. Fluid Mech.* **356**, 25–64.
- MONKEWITZ, P. A. 1988 Subharmonic resonance, pairing and shredding in the mixing layer. *J. Fluid Mech.* **188**, 223–252.
- PAPAMOSCHOU, D. & BUNYAJITRADULYA, A. 1997 Evolution of large eddies in compressible shear layers. *Phys. Fluids* **9**, 756–765.
- PAPAMOSCHOU, D. & ROSHKO, A. 1988 The compressible turbulent shear layer: an experimental study. *J. Fluid Mech.* **197**, 453–477.
- PAPAS, P., MONKEWITZ, P. A. & TOMBOULIDES, A. G. 1999 New instability modes of a diffusion flame near extinction. *Phys. Fluids* **11**, 2818–2820.

- PLANCHÉ, O. H. 1992 A numerical investigation of the compressible reacting mixing layer. PhD thesis, Stanford University, Stanford, CA 94305.
- PLANCHÉ, O. H. & REYNOLDS, W. C. 1992 A numerical investigation of the compressible reacting mixing layer. *Rep. TF-56*, Mechanical Engineering Department, Stanford University.
- PLANCHÉ, O. H. & REYNOLDS, W. C. 1992 Heat release effects on mixing in supersonic reacting free shear-layers. *AIAA Paper* 92-0092.
- ROGERS, M. & MOSER, R. D. 1994 Direct simulation of a self-similar turbulent mixing layer. *Phys. Fluids* **6**, 903–923.
- ROSSMANN, T., HANSON, R. K. & MUNGAL, M. G. 1999 A new shock tunnel facility for high compressibility mixing layer studies. *AIAA Paper* 99-0415.
- SANDHAM, N. D. 1989 A numerical investigation of the compressible mixing layer: linear theory and direct simulation. PhD thesis, Stanford University, Stanford, CA 94305.
- SANDHAM, N. D. 1994 The effect of compressibility on vortex pairing. *Phys. Fluids* **6**, 1063–1072.
- SANDHAM, N. D. & REYNOLDS, W. C. 1989 A numerical investigation of the compressible mixing layer: linear theory and direct simulation. *Rep. TF-45*, Mechanical Engineering Department, Stanford University.
- SANDHAM, N. D. & REYNOLDS, W. C. 1991 Three-dimensional simulations of large eddies in the compressible mixing layer. *J. Fluid Mech.* **224**, 133–158.
- SCHLICHTING, H. 1979 *Boundary-Layer Theory*, 7th Edn. McGraw-Hill.
- SHIN, D. S. & FERZIGER, J. H. 1993 Linear stability of the compressible reacting mixing layer. *AIAA J.* **31**, 677–685.
- SMITH, K. M. & DUTTON, J. C. 1999 Evolution and convection of large-scale structures in supersonic reattaching shear flows. *Phys. Fluids* **11**, 2127–2138.
- VREMAN, A. W., SANDHAM, N. D. & LUO, K. H. 1996 Compressible mixing layer growth rate and turbulence characteristics. *J. Fluid Mech.* **320**, 235–258.
- WILLIAMS, F. A. 1985 *Combustion Theory*. Benjamin/Cummings.
- WINANT, C. D. & BROWAND, F. K. 1974 Vortex pairing. *J. Fluid Mech.* **63**, 237–255.